

# Filling in CMB map missing data using constrained Gaussian realizations

Martin Bucher<sup>1\*</sup> and Thibaut Louis<sup>1,2,3†</sup>

<sup>1</sup>*Laboratoire Astroparticule & Cosmologie, Université Paris Diderot 7, 10 rue Alice Domon et Léonie Duquet, 75013 Paris, France*

<sup>2</sup>*Laboratoire de Physique, ENS de Lyon, 46, allée d'Italie F69007 Lyon, France*

<sup>3</sup>*Oxford Astrophysics, Department of Physics, Denys Wilkinson Building, Keble Road, Oxford OX1 3RH, UK*

1 September 2011; revised 11 September 2011

## ABSTRACT

For analyzing maps of the cosmic microwave background sky, it is necessary to mask out the region around the Galactic equator where the parasitic foreground emission is strongest as well as the brightest compact sources. Since many of the analyses of the data, particularly those searching for non-Gaussianity of a primordial origin, are most straightforwardly carried out on full-sky maps, it is of great interest to develop efficient algorithms for filling in the missing information in a plausible way. In this paper we explore algorithms for filling in based on constrained Gaussian realizations. Although carrying out such realizations is in principle straightforward, for finely pixelized maps as will be required for the Planck analysis a direct brute force method is not numerically tractable. Here we present some concrete solutions to this problem, both on a spatially flat sky with periodic boundary conditions and on the pixelized sphere. One approach is to solve the linear system with an appropriately preconditioned conjugate gradient method. While this approach was successfully implemented on a rectangular domain with periodic boundary conditions and worked even for very wide masked regions, we found that the method failed on the pixelized sphere for reasons that we explain here. We present an approach that works for full-sky pixelized maps on the sphere involving a kernel-based multi-resolution Laplace solver followed by a series of conjugate gradient corrections near the boundary of the mask.

## 1 INTRODUCTION

The analysis of the anisotropies both in temperature and polarization of the primeval cosmic microwave background has contributed substantially to our present understanding of the Universe on the largest scales and at the earliest times and continues to be an area of intense activity. According to the simplest inflationary models, the primordial cosmological perturbations should be very nearly Gaussian. Consequently much of the focus has been on exploiting the power spectrum, which for an isotropic Gaussian underlying statistical process would encapsulate all the exploitable information. Initial studies of CMB maps indeed show that any non-Gaussianity that may be present in the primordial signal must be very small. Nevertheless tests of non-Gaussianity provide a powerful test of the current cosmological paradigm and of possible new physics, and inflationary models do exist predicting levels of non-Gaussianity that will be measurable with the Planck space mission and other new data sets.

One of the obstacles to characterizing the primordial CMB anisotropies is the emission from Galactic and extragalactic foregrounds. Indeed how best to separate and remove these foregrounds is an area of intense activity. However near the Galactic plane and in the immediate vicinity of strong point sources, the best strategy is to mask these regions, giving sky maps with a cut around the Galactic equator of varying width and numerous holes. Theoretical models are best analyzed in terms of full-sky maps, so given this situation, there are two alternatives: (1) one can adapt estimators to cut sky maps, although doing so often involves linear algebra problems that are ill-conditioned and numerically extremely demanding, (2) one can fill-in the maps with various algorithms to obtain a plausible full-sky map and then analyze these using full-sky algorithms. The philosophy behind approach (2) is somewhat suspect and studies, for example by Monte Carlo, of the effect

or possible artifacts of the filling in algorithm are required. Nevertheless, if the underlying statistical process is not far from Gaussian and the fraction of the sky masked out is small, one would expect the error to be minimal and characterizable.

Several algorithms have been proposed to fill-in maps. (This process is sometimes called ‘in-painting.’) Abrial et al. (2007, 2008); Perotto et al. (2010) for example have proposed using techniques based on sparsity that have proved remarkably successful for restoring images from photographs that have been blurred and have a large number of missing pixels. This technique has the advantage that it does not require any assumptions regarding the underlying power spectrum. However one drawback of this approach is that it is difficult to know whether these techniques might introduce parasite non-Gaussianity not already present in the original maps. In this paper we instead consider filling in by means of constrained Gaussian realizations. Under this approach it is assumed that the power spectrum can be characterized sufficiently well based on the data from the unmasked pixels. Then a random map is generated taking the observed pixels as given. Let us denote a sky map by the vector in block form  $\mathbf{z} = (\mathbf{x}, \mathbf{y})$  where  $\mathbf{x}$  corresponds to those fixed which have been masked, or not observed, and  $\mathbf{y}$  corresponds to those pixels that have been observed, or not masked. We assume that the joint distribution is given by a Gaussian distribution  $P(\mathbf{z}) = (2\pi)^{-n_{pix}/2} \det^{-1/2}[\mathbf{C}] \exp[-\frac{1}{2}\mathbf{z}^T \mathbf{C}^{-1} \mathbf{z}]$  and wish to fill-in based on the conditional probability distribution  $P(\mathbf{x}|\mathbf{y})$ . Formally the problem may be solved almost trivially using elementary matrix algebra and the solution reduces to the form  $P(\mathbf{x}|\mathbf{y}) = (2\pi)^{-n_{masked}/2} \det^{-1/2}[\mathbf{C}_{const}] \exp[-(1/2)(\mathbf{x} - \mathbf{x}_{ML})^T \mathbf{C}_{const}^{-1} (\mathbf{x} - \mathbf{x}_{ML})]$  where  $\mathbf{C}_{const} = \mathbf{C}_{\mathbf{xx}}^{-1}$  and  $\mathbf{x}_{ML} = ((\mathbf{C}^{-1})_{\mathbf{xx}})^{-1} (\mathbf{C}^{-1})_{\mathbf{xy}} \mathbf{y}$ . The maximum likelihood map in a cut region is essentially a Wiener filter as discussed in the context of CMB maps by Bunn, Hoffman & Silk (1996, 1994); Bunn et al. (1994). (For a more recent discussion of some related issues see Feeney et al. (2011).) If the number of pixels in a map were modest, a direct solution would be trivial. However for CMB maps of the resolution needed for Planck, one has typically up to  $5 \times 10^7$  pixels (corresponding to a Healpix map with  $n_{side} = 2048$ ), so operations of order  $n_{pix}^2$  are to be avoided if at all possible, and operations of order  $n_{pix}^3$  such as would be required to solve a linear system directly or to invert a matrix are ruled out. While  $\mathbf{C}^{-1}$  may take a particularly simple form over the full sky, for example when both the underlying cosmological model and the instrument noise are isotropic, the presence of the projection operators onto the masked and unmasked regions breaks this isotropy, introducing nonzero off-diagonal elements almost everywhere. Moreover because of the nearly scale invariant nature of the underlying spectrum, the matrices are poorly conditioned.

There is some overlap between this work and studies of Gibbs sampling for CMB power spectrum estimation as discussed for example in Wandelt, Larson & Lakshminarayanan (2004); Eriksen et al. (2004, 2008). Here one of the steps in the Gibbs sampling loop is to generate a map for the underlying CMB anisotropies  $s$  according to the conditional distribution  $P(s|P, m)$  where  $P$  is the assumed power spectrum and  $m$  is the maximum-likelihood map (resulting as an output from a map maker program) whose deviations from  $s$  are described by the inverse noise matrix  $N^{-1}$ . Under this approach foregrounds may either be incorporated into  $N^{-1}$  or  $(N^{-1})_{aa}$  (where  $a$  is the pixel index) may be set to zero, which has the effect of masking out those pixels. Another related filling in approach called ‘harmonic inpainting’ Inoue, Cabella, & Komatsu (2008). This last approach is somewhat ad hoc but has been shown to yield reasonable results.

Some issues associated with constrained Gaussian realizations have been discussed in Cardoso & Prunet (1994). We are aware of a number of private codes for carrying out constrained Gaussian realizations on the sphere, in many cases only with coarser pixelizations. However at present no systematic discussion of this problem seems to exist in the literature. This paper endeavors to fill this gap. We found the related papers of Hoffman & Ribak (1991) and ? useful.

The organization of the paper is as follows. In Section 2 we explore a solution based on the conjugate gradient method. The problem as formally presented above can be divided into two operations: (1) given a  $\mathbf{y}$  calculating  $\mathbf{x}_{ML}$ , and (2) producing a random vector  $\delta x$  whose covariance matrix is  $\mathbf{C}^{-1}_{\mathbf{xx}}$ . Operation (2) is not necessarily trivial when the dimension is large and  $\mathbf{C}^{-1}_{\mathbf{xx}}$  has a lot of diagonal elements. We show how using a trick due to Hoffman & Ribak (1991), instead of carrying out (1)+(2), the procedure can be simplified by carrying out a random realization over the whole sky, followed by (1) acting on  $\mathbf{y}$  plus another component. It is shown how (1) can be pre-conditioned so that a conjugate gradient solution converges rapidly. A numerical demonstration is carried out on the torus and several tests are performed to validate the solution. We present an alternative method using a kernel-based, multi-scale Laplace solver to fill the widest gaps followed by a series of conjugate gradient improvement in increasingly narrow strips around the mask boundary. Section 3 discusses a numerical implementation of a preconditioned conjugate gradient method on a toroidal domain. Section 4 discusses some of the difficulties related to spherical harmonic transform on the pixelized sphere particularly near the angular scale of the pixelization. Section 5 presents an integral equation formulation of the filling in problem in angular space examining the properties of the kernels first for a toy model and then for more realistic situations. Section 6 presents an alternative procedure for filling in on the pixelized sphere and Section 7 closes with a few concluding comments.

## 2 CONSTRAINED GAUSSIAN REALIZATIONS

### 2.1 Mathematical formulation

In the previous section we saw that there is considerable interest in finding a suitable way to fill in missing data so that full sky filtering could be carried out and then masks could be reapplied in order to minimize the artifacts of this filling in. Such filling in is inevitably dangerous as the filled in data is likely to bias the measured non-Gaussianity

In a constrained Gaussian realization, we assume that the power spectrum of the underlying cosmological model and of the noise is known with sufficient precision. We generate a random realization according to this distribution while constraining the data in the unmasked region to take its observed value. Schematically we may write the probability distribution in pixel space as  $\mathbf{z} = (\mathbf{x}, \mathbf{y})^T$ . We have

$$P(\mathbf{z}) \propto \exp \left[ -\frac{1}{2} \mathbf{z}^T (\mathbf{P} + \mathbf{N})^{-1} \mathbf{z} \right] \quad (1)$$

where  $\mathbf{P}$  is Gaussian primordial power spectrum and  $\mathbf{N}$  is the instrument noise superimposed. Setting  $\mathbf{C}^{-1} = (\mathbf{P} + \mathbf{N})^{-1}$ , we obtain

$$\begin{aligned} P(\mathbf{z}) &\propto \exp \left[ -\frac{1}{2} \begin{pmatrix} \mathbf{x} \\ \mathbf{y} \end{pmatrix}^T \begin{pmatrix} (\mathbf{C}^{-1})_{\mathbf{x}\mathbf{x}} & (\mathbf{C}^{-1})_{\mathbf{x}\mathbf{y}} \\ (\mathbf{C}^{-1})_{\mathbf{y}\mathbf{x}} & (\mathbf{C}^{-1})_{\mathbf{y}\mathbf{y}} \end{pmatrix} \begin{pmatrix} \mathbf{x} \\ \mathbf{y} \end{pmatrix} \right] \\ &\propto \exp \left[ -\frac{1}{2} \left( \mathbf{x}^T (\mathbf{C}^{-1})_{\mathbf{x}\mathbf{x}} \mathbf{x} + \mathbf{x}^T (\mathbf{C}^{-1})_{\mathbf{x}\mathbf{y}} \mathbf{y} + \mathbf{y}^T (\mathbf{C}^{-1})_{\mathbf{y}\mathbf{x}} \mathbf{x} \right) \right] \\ &\propto \exp \left[ -\frac{1}{2} \left( (\mathbf{x} - \mathbf{x}_{ML})^T (\mathbf{C}^{-1})_{\mathbf{x}\mathbf{x}} (\mathbf{x} - \mathbf{x}_{ML}) \right) \right] \end{aligned} \quad (2)$$

where

$$\mathbf{x}_{ML} = -((\mathbf{C}^{-1})_{\mathbf{x}\mathbf{x}})^{-1} (\mathbf{C}^{-1})_{\mathbf{x}\mathbf{y}} \mathbf{y} = -(\mathcal{P}_x \mathbf{C}^{-1} \mathcal{P}_x)^{-1} (\mathcal{P}_x \mathbf{C}^{-1} \mathcal{P}_y) \mathbf{y} = \mathbf{M}\mathbf{y} \quad (3)$$

where  $\mathcal{P}_x$  and  $\mathcal{P}_y$  are the projection operators onto the unobserved (masked) and observed (constrained) pixels, respectively.

For  $\mathbf{y}$  fixed, the  $\mathbf{x}$  of the constrained realization decomposes as

$$\mathbf{x} = \mathbf{x}_{ML} + \mathbf{x}_R \quad (4)$$

where  $\mathbf{x}_{ML}$  is the deterministic part and  $\mathbf{x}_R$  is the random contribution of vanishing mean everywhere. Here ML stands for maximum likelihood.

### 2.2 Qualitative behavior: an exactly solvable toy model

Before proceeding to the technical details of a practical and efficient implementation for generating constrained Gaussian realizations, in order to provide some intuition we briefly describe qualitatively what the fields  $\mathbf{x}_{ML}$  and  $\mathbf{x}_R$  typically look like in the masked region. If we assume an exactly scale-invariant spectrum for the primordial contribution  $\mathbf{P}$  (i.e.,  $P(\ell) \sim \ell^{-2}$ ) and no noise (i.e.,  $N(\ell) = 0$ ), then  $C(\ell) = P(\ell) + N(\ell) \sim \ell^{-2}$ , and in this idealized case  $\mathbf{C}^{-1}$  is simply the two-dimensional Laplacian operator  $\nabla^2$ . It follows that in the masked region  $\nabla^2 T = 0$  and Dirichlet boundary conditions are imposed with  $T$  fixed on the boundary, which in this idealized case is of zero breadth, to the values in the unmasked region at the boundary. For a circular hole of radius  $a$ , we obtain the following maximum likelihood (ML) extrapolation of the temperature map  $T$  into the interior (where  $\rho < a$ )

$$T(\rho, \theta) = \sum_{-\infty}^{+\infty} \left( \frac{\rho}{a} \right)^{|m|} \int_0^{2\pi} \frac{d\theta'}{2\pi} \exp [im(\theta - \theta')] T(a, \theta'), \quad (5)$$

so that the value at the center is the average and the small scale structure on the boundary decays as one moves inward toward the center of the hole. When the boundary curvature is ignored, solutions have the form  $\exp[ik\theta] \exp -|k|(a - r)$  just inside.

In the presence of white noise (from the instrument), the effective boundary fattens. When there is white noise, the value measured at the boundary is meaningless because it is infinitely noisy, and one must average outward a distance of order  $\theta_{eq} \approx \ell_{eq}^{-1}$  (where  $\ell_{eq}$  is the multipole number at which the white noise and primordial signal are equal). In this case, eqn. (5) is replaced with

$$T(\rho, \theta) = \sum_{-\infty}^{+\infty} \left( \frac{\rho}{a} \right)^{|m|} \int_0^{2\pi} \frac{d\theta'}{2\pi} \int_a^\infty d\rho' \exp [im(\theta - \theta')] K_m(\rho; \rho') T(a, \theta'), \quad (6)$$

and where  $(\rho' - a)/\theta_{eq} \gg 1$  the kernel contributes negligibly. As the noise is increased, the support of the kernel spreads outward into the unmasked region.

Concerning the random component  $\mathbf{x}_R$ , on small scales and near the center of the hole, the fluctuations are almost as for an unconstrained realization over both the masked and unmasked domain. But closer to the boundary fluctuations are suppressed because some of the fluctuations outside propagate inward through the evolution of  $\mathbf{x}_{ML}$  described above. Almost all the fluctuations on scales larger than the dimension of the hole propagate in through  $\mathbf{x}_{ML}$ . In the presence of noise, however, fluctuations much smaller than  $\theta_{eq}$  are only weakly suppressed as one approaches the boundary.

Here we have considered the special case where  $P$  is exactly scale invariant. For deviations from scale invariance one expects the kernel to fan out, even in the absence of noise. The infinitely thin boundary dependence is an artifact of exact scale invariance.

### 2.3 Efficient computation of random component

We would like to generate in an efficient way realizations of the random component  $\mathbf{x}_R$  of the constrained Gaussian realization with zero mean and covariance matrix

$$((\mathbf{C}^{-1})_{xx})^{-1} = \mathbf{C}_{xx} - \mathbf{C}_{xy}\mathbf{C}_{yy}^{-1}\mathbf{C}_{yx}. \quad (7)$$

Generating a random vector with a generic covariance matrix of large dimension is a costly operation in the generic case. The first step involves finding the Cholesky decomposition of the covariance matrix  $\mathbf{C} = \mathbf{G}\mathbf{G}^T$  (i.e., the moral equivalent of taking the square root of a symmetric matrix) where  $\mathbf{G}$  is lower triangular with strictly positive diagonal entries. This calculation would involve  $O(N^3)$  operations as would matrix inversion. Once the Cholesky decomposition has been calculated, successive realizations would cost  $O(N^2)$  because the bottleneck now is simply a matrix multiply.

This brute force approach can be avoided using a simple trick due to Hoffman & Ribak (1991). If we create a joint random realization of  $(\mathbf{x}, \mathbf{y})$  on the full sphere with covariance matrix

$$\mathbf{C} = \begin{pmatrix} \mathbf{C}_{xx} & \mathbf{C}_{xy} \\ \mathbf{C}_{yx} & \mathbf{C}_{yy} \end{pmatrix}, \quad (8)$$

which is easy because there are no cuts to break the isotropy, then the random variable

$$\mathbf{x}' = \mathbf{x} - \mathbf{M}\mathbf{y} \quad (9)$$

has a covariance matrix equal to

$$\mathbf{C}_{xx} - \mathbf{M}\mathbf{C}_{yx} - \mathbf{C}_{xy}\mathbf{M}^T + \mathbf{M}\mathbf{C}_{yy}\mathbf{M}^T, \quad (10)$$

which for  $\mathbf{M} = \mathbf{C}_{xy}(\mathbf{C}_{yy})^{-1}$  yields  $\mathbf{C}_{xx} - \mathbf{C}_{xy}(\mathbf{C}_{yy})^{-1}\mathbf{C}_{yx}$ , which is precisely the desired correlation matrix given in eqn. (7). Here we have used the block decomposition relation

$$\begin{pmatrix} \mathbf{A}_{xx} & \mathbf{A}_{xy} \\ \mathbf{A}_{yx} & \mathbf{A}_{yy} \end{pmatrix}^{-1} = \begin{pmatrix} [\mathbf{A}_{xx} - \mathbf{A}_{xy}(\mathbf{A}_{yy})^{-1}\mathbf{A}_{yx}]^{-1} & [\mathbf{A}_{xx} - \mathbf{A}_{xy}(\mathbf{A}_{yy})^{-1}\mathbf{A}_{yx}]^{-1}\mathbf{A}_{xy}(\mathbf{A}_{yy})^{-1} \\ [\mathbf{A}_{yy} - \mathbf{A}_{yx}(\mathbf{A}_{xx})^{-1}\mathbf{A}_{xy}]^{-1}\mathbf{A}_{yx}(\mathbf{A}_{xx})^{-1} & [\mathbf{A}_{yy} - \mathbf{A}_{yx}(\mathbf{A}_{xx})^{-1}\mathbf{A}_{xy}]^{-1} \end{pmatrix} \quad (11)$$

which holds when  $\mathbf{A}_{xx}$  and  $\mathbf{A}_{yy}$  are invertible, which is always the case when  $\mathbf{A}$  is positive definite. The same relation gives the equality  $\mathbf{C}_{xy}\mathbf{C}_{yy}^{-1} = ((\mathbf{C}^{-1})_{xx})^{-1}((\mathbf{C}^{-1})_{xy})$ . Note that  $\mathbf{M}$  here is identical to the operator yielding  $\mathbf{x}_{ML}$  given values  $\mathbf{y}$  in the unmasked region. Consequently all the difficulty of generating random realizations reduces to the operation of finding  $\mathbf{x}_{ML}$  given  $\mathbf{y}$ .

### 2.4 Conjugate gradient solution and an effective preconditioner

The conjugate gradient method, first introduced by Hestenes & Stiefel 1952 (see also Golub & Van Loan 1996 for a nice review), solves linear equations of the form  $\mathbf{A}\mathbf{x} = \mathbf{y}$  (where in the original and simplest case  $\mathbf{A}$  is symmetric and positive definite). The conjugate gradient method yields a sequence of successive approximations to the exact solution by forming linear combinations of  $\mathbf{y}, \mathbf{A}\mathbf{y}, \mathbf{A}^2\mathbf{y}, \dots, \mathbf{A}^{j-1}\mathbf{y}$ . The condition number, defined as  $\kappa(\mathbf{A}) = \|\mathbf{A}\| \|\mathbf{A}^{-1}\|$  (where  $\|\mathbf{T}\| = \sup_{\mathbf{x} \neq \mathbf{0}} \|\mathbf{T}\mathbf{x}\|/\|\mathbf{x}\|$ ) or the ratio of moduli of the largest to smallest eigenvalues, plays an important role in determining the rate of convergence of these successive approximations. If  $\kappa(\mathbf{A})$  is not too much larger than one, the sequence rapidly converges and a good approximation is had after a modest number of steps. While the smallness of the condition number is a sufficient condition for rapid convergence, good convergence properties also follow if all but a few eigenvalues are clustered closely together. The fast convergence for small condition number is easy to understand because in terms of the eigenvalues one is essentially approximating the real function  $f(\lambda) = 1/\lambda$  on the interval  $[1, \kappa]$  by means of successively higher order polynomials.

For a linear system of dimension  $N$ , the conjugate gradient method is guaranteed to converge after  $N$  steps for any value of the condition number. But this property is not very useful because multiplying by  $\mathbf{A}$  generically involves  $O(N^2)$  operations, so continuing for  $N$  iterations would involve  $O(N^3)$  operations, which is the same order as a direct method (e.g., Gaussian elimination). On the other hand, for well-conditioned matrices the speedup resulting from the conjugate gradient method is considerable, especially in high dimension. When the matrix can be applied to a vector using less than  $O(N^2)$  operations (e.g., because of sparsity or some other reason), the speedup is even more dramatic.

For our problem,  $N \propto n_{side}^2$ . The projection by a mask or its complement entails  $O(N)$  operations. Applying the FFT on the rectangular or toroidal region and spherical harmonic transform require  $O(N \log N)$  and  $N^{3/2} \log N$  operations, respectively [Gorski et al. (2005)]. Therefore solving the problem

$$(\mathcal{P}_x \mathbf{C}^{-1} \mathcal{P}_x) \mathbf{u} = \mathbf{v} \quad (12)$$

would be ideally suited to the conjugate gradient method if it were not for the fact that  $(\mathcal{P}_x \mathbf{C}^{-1} \mathcal{P}_x)$  is extremely ill-conditioned. We estimate the condition number  $\kappa(\mathbf{C})$ . Here  $\mathbf{C} = \mathbf{P} + \mathbf{N}$  where  $\mathbf{P}$  very roughly has a scale invariant spectrum (with  $P(\ell) \propto \ell^{-2}$ ) and  $\mathbf{N}$  has a white noise spectrum (with  $N(\ell) = (\text{constant})$ ). Let  $\ell_{eq}$  denote the multipole number where the noise roughly equals the primordial signal. It follows that  $\kappa(\mathbf{C}^{-1})$  is approximately  $(\ell_{eq}/\ell_{min})^2$  no matter how fine the pixelization is. The noise serves as a cut-off preventing the small scale eigenvalues from becoming too extreme. This estimate is not very accurate, but there is no sense in trying to do better because its value is so extreme (i.e.,  $\gtrsim 10^6$  for Planck) that the conjugate gradient method on this problem in its present state will not converge fast enough.

We try to improve the problem by means of a pre-conditioner by rewriting eqn. (12) as

$$(\mathcal{P}_x C^{1/2} \mathcal{P}_x)(\mathcal{P}_x \mathbf{C}^{-1} \mathcal{P}_x)(\mathcal{P}_x C^{1/2} \mathcal{P}_x) \mathbf{u}' = (\mathcal{P}_x C^{1/2} \mathcal{P}_x) \mathbf{v} = \mathbf{v}' \quad (13)$$

or

$$\mathbf{M}' \mathbf{u}' = (\mathcal{P}_x \mathbf{C}^{1/2} \mathcal{P}_x \mathbf{C}^{-1} \mathcal{P}_x \mathbf{C}^{1/2} \mathcal{P}_x) \mathbf{u}' = \mathbf{v}' \quad (14)$$

Here  $\mathbf{v}'$  is easy to obtain from  $\mathbf{v}$  and so is  $\mathbf{u}$  from  $\mathbf{u}'$ . Since the powers of  $\mathbf{C}$  add up to zero, one would hope that the eigenvalues of the entire product would cluster near unity, but the projection operators, which act in real rather than harmonic space, could act to spoil this attempt to improve the conditioning of the matrix. The sharp boundaries imposed by the projection operator convert low- $\ell$  modes into a superposition containing some high- $\ell$  modes (because the initial data to which  $C^{-1}$  is applied is taken to vanish on the complement of  $\mathbf{x}$ ). Similarly, in the other direction, the projection operator also partially converts high- $\ell$  modes into high- $\ell$  modes. Therefore if mixing were strong enough one could expect eigenvalue of order  $\lambda_{max}/\lambda_{min}$  and  $\lambda_{min}/\lambda_{max}$  where  $\lambda$  refers to the eigenvalues of  $C$ . Rather than seeking more sophisticated analytic estimates of the condition number and convergence rate of this pre-conditioned system, we explore the convergence by numerical experiment in the next section.

### 3 PRECONDITIONED CONJUGATE GRADIENT APPROACH ON A PERIODIC FLAT DOMAIN

For high resolution experiments, such as ACT [Das et al. (2010); Dunkley et al. (2010)] and SPT [Keisler, Reichardt et al. (2011)], which maps the small scale anisotropies of the CMB on small patches of the sky, it is convenient to use the flat sky approximation, where the analysis of the CMB is made on a torus. We decide to test our implementation using the characteristics of an ACT-like experiment. The power spectrum of the survey is given by a combination of the underlying power spectrum modified by the beam profile coefficients  $\omega_\ell$  and a white noise term

$$P_\ell = \omega_\ell C_\ell + N_\ell \quad (15)$$

We simulated 4 CMB maps of  $7000 \times 600$  pixels using this distribution, each of them corresponding to a season of observation of 300 square degrees of the sky. We applied a realistic point source mask ( $\approx 400$  holes of area  $10^{-2}$  degree square) to the maps. When we apply a point source mask to a map, we replace the pixel values in an area containing each point source with zeros. CMB power spectrum estimated from an incomplete sky map is the underlying full-sky power spectrum convolved with the power spectrum of the mask. This leads to coupling of modes in the estimated power spectrum. The mask becomes even more problematic in the context of lensing power spectrum and bispectrum estimation. We show the result of one reconstruction in Fig. 1.

As expected, the continuity is well preserved, the temperature scale is the same as that of the initial map and the perimeter of the cut is not visible. The conjugate gradient algorithm converges extremely quickly, with the residues following a geometrical progression. For filling in a point source mask, the use of a preconditioner is unnecessary. We define the residual for each iteration as  $\mathbf{r}_{(i)} = \mathbf{y} - \mathbf{A}\mathbf{x}_{(i)}$ . We found that the norm of the residual decayed by about a factor of two per iteration. The reconstruction for one map is then complete in 20 minutes using one processor.

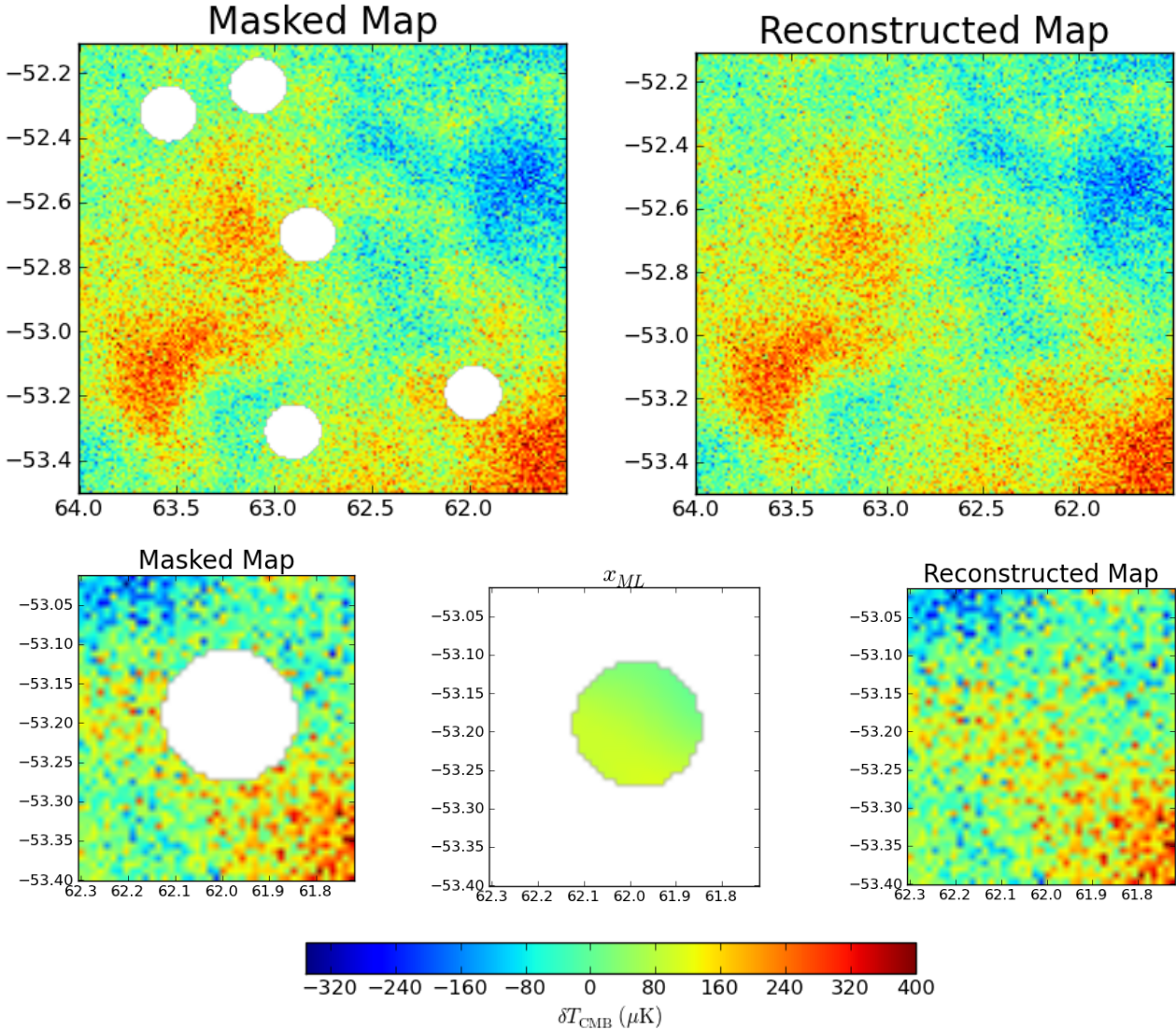


**Figure 1. Conjugate gradient reconstruction of mask regions of mock ACT data.** (Top) The constraints, given by the masked map, and the map reconstructed by the mean of Gaussian Constraint realization for a zoom on a 2.1 degree square part of the map, the coordinates are given in decimal degree. (Bottom) we zoom on a typical mask hole, in a region of 0.13 square degree, at the center we show the maximum likelihood solution which propagates the information into the hole

The typical size of the hole is given in angular space by  $\ell \approx \pi/\theta$  where  $\theta$  is the radius of the hole. Here  $\ell \approx 3600$ , which lies deep in the noise dominated part of the spectrum indicated. This implies that the maximum likelihood part of the reconstruction mainly continues the average temperature and its gradient into the hole here.

Fig. 2 shows the reconstruction of a  $30^\circ$  wide Galactic type mask, using  $N_x = 4N_{side}$  pixels in the horizontal direction with  $N_{side} = 2048$ . The use of a preconditioner for filling in a wide mask is a necessary condition to achieve the convergence in a reasonable amount of time (6 hours of computer time with one processor). Fig. 3 shows the maximum likelihood reconstruction on a square subregion of the Galactic cut, enlightening the structural difference between the boundary layer and the deep interior.

The procedure for filling in on the torus described in this section was applied to the sphere pixelized using the Healpix package and in particular the forward and inverse spherical harmonic transforms provided in that package. With parameters chosen identical to those for the torus, we found that the iterations of the conjugate gradient solver did not converge. Although a direct proof is lacking, we strongly suspect that this failure is due to the lack of Hermiticity of the operators when approximated using Healpix, under which the harmonic transform followed by its inverse does not recover the identity operator exactly. We performed some simulations where the standard conjugate gradient algorithm was applied to matrices with deviations from perfect Hermiticity. We found that for modest condition numbers  $\kappa \lesssim 100$ , deviations had to be around

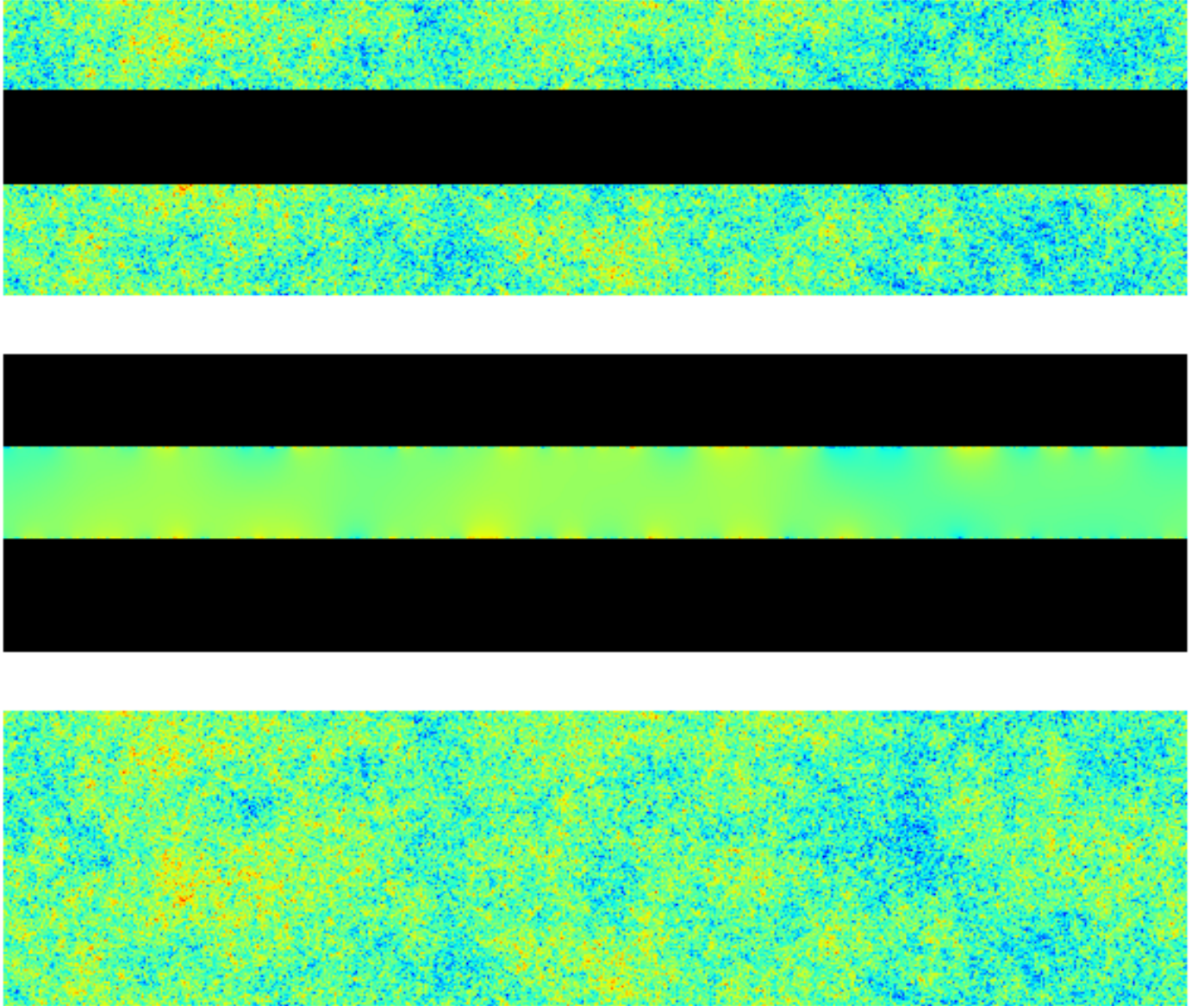


**Figure 2. Reconstruction of Galactic cut** In the original map (top panel) the pixels in a strip  $30^\circ$  wide along the Galactic plane has been masked (shown in black). The middle panel shows the maximum likelihood reconstruction of the missing pixels based on the unmasked pixels in the panel above. In the lower panel show a full reconstruction using a constrained Gaussian realization, assuming the underlying power spectrum is known.

10%, before the lack of Hermiticity spoiled or significantly slowed down convergence. However for larger condition numbers, much smaller departures from Hermiticity were found to spoil convergence. In this case, the rate of convergence (expressed as  $-\ln(\|r_{n+1}\|/\|r_n\|)$ ) would decrease with successive iterations and approach zero rather than fluctuating around a constant positive value. It could well be that a modification of Healpix might remedy this difficulty, but below we describe another strategy demonstrated to work on the sphere.

We note that for solving  $Ax = y$  a number of variations have been proposed to the classical conjugate gradient method of Hestenes and Stiefel where  $A$  is assumed symmetric and positive definite. When  $A^T$  is likewise easily calculable, one can use the biconjugate gradient method, where there is no assumption of Hermiticity [Fletcher 1976]. Unfortunately, there is no easy way of applying  $A^T$  to an arbitrary vector. Other Krylov space methods rely on calculating a number of inner products of order the square of the number of iterations, and thus become impractical both because of storage requirements and because of the number of operations required.

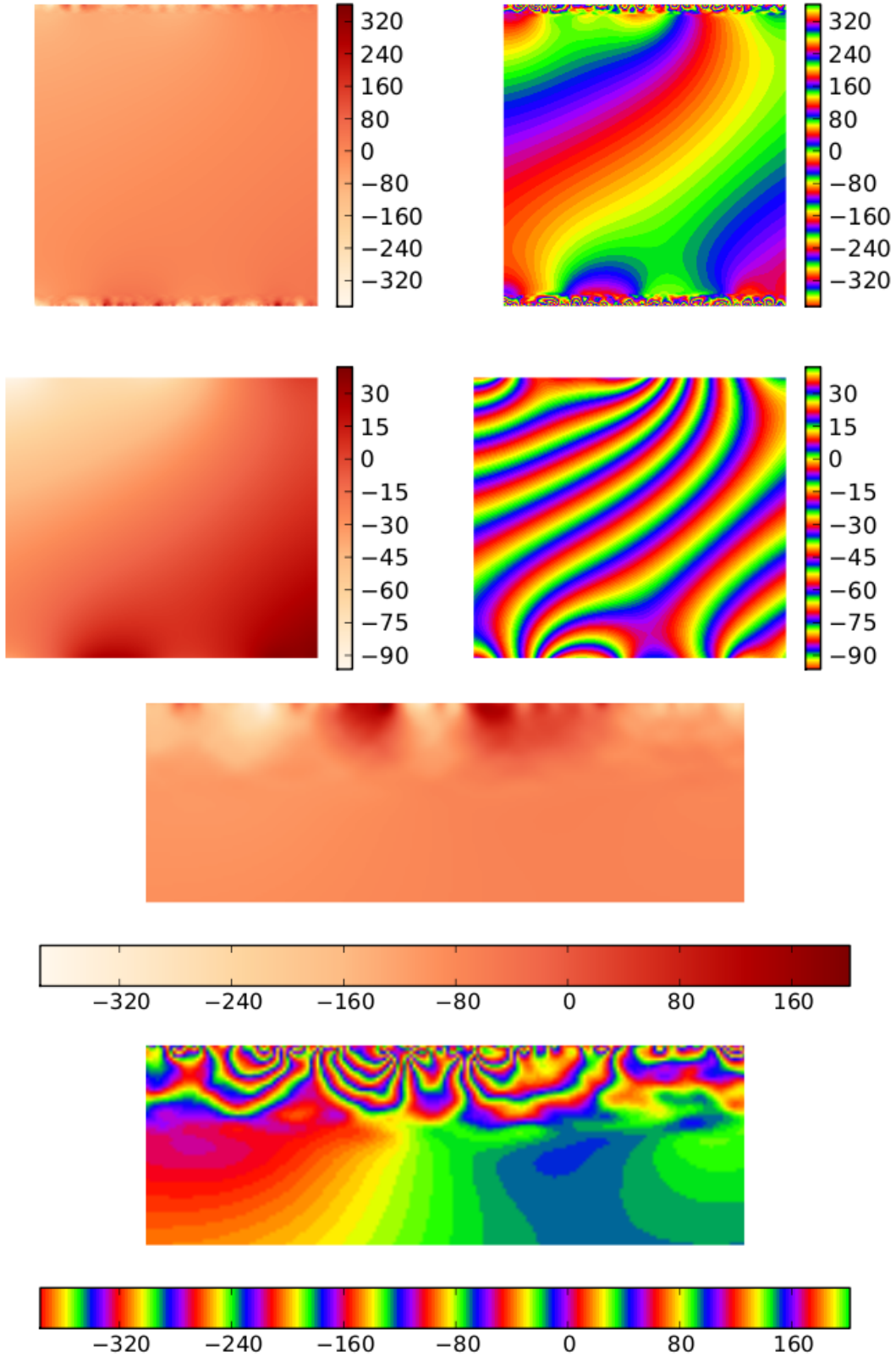


**Figure 3. Maximum likelihood reconstruction of the Galactic cut.** The top row shows the maximum likelihood reconstruction of a square subregion of the Galactic cut using two color scales, a simple scale on the left to provide a global view and a periodic scale on the right to highlight the contours of constant value and nature of the variation in the central region. In the second row the boundary region where the variation is greatest has been cut away to accentuate the nature of the variation in the central region, which we call the “deep interior.” The bottom row shows a zoom of the boundary region, where the distinction between the boundary layer and the deep interior is clearly visible.

#### 4 PIXELIZATION ERRORS ON THE SPHERE

In this section we explore some of the obstacles to extending the conjugate gradient approach that worked so well on the torus to the sphere. As we shall investigate in more detail, many of the nice properties of the FFT on a rectangular or periodic lattice do not carry over to the pixelized sphere, and it is these differences that prevent the constrained Gaussian realizations that worked so well on the torus from working equally well on the sphere.

On the torus (i.e., a rectangle with periodic boundary conditions imposed) for a representation of the circle using  $N$  equally spaced points, the discrete Fourier transform has the property that

$$\mathcal{F}_N^\dagger \mathcal{F}_N = I_N$$

holds exactly and not just approximately. Here  $I_N$  is the identity operator on the  $N$ -dimensional vector space. Mathematically, the fact that  $\{U(1)\}^d$  can be approximated by the sequence  $\{Z_N\}^d$  as  $N \rightarrow \infty$  is at the heart of this property. There thus exists a sequence of arbitrarily fine tilings of  $\{U(1)\}^d$ , or equivalently of the  $d$ -dimensional torus.

The same does not hold for the sphere. Except for the two infinite series of symmetry groups  $C_N$  and  $D_N$  (corresponding to the cyclic and dihedral groups of order  $N$  and  $2N$ , respectively), the finite order subgroups of  $SO(3)$  are finite in number. The remaining groups are the tetrahedral (T), octahedral (O), and icosahedral (I) groups and can be placed in correspondence with the platonic solids.  $T$  is the symmetry group of the tetrahedron,  $O$  of the cube and octahedron, and  $I$  of the dodecahedron (12 sides) and icosahedron (20 sides). This situation severely limits the regular tilings of the sphere. The  $C$  and  $D$  series are not useful because the pixels become finer only in one dimension.

On the sphere we would like to generalize the continuum resolution of unity

$$\sum_{\ell=0}^{\infty} \sum_{m=-\ell}^{+\ell} Y_{\ell m}^*(\hat{\Omega}) Y_{\ell m}(\hat{\Omega}') = \delta^2(\hat{\Omega}, \hat{\Omega}') \quad (16)$$

where  $\delta^2(\hat{\Omega}, \hat{\Omega}') = \delta(\theta - \theta')\delta(\phi - \phi')/\sin\theta$ , to something like

$$\sum_{\ell=0}^{\ell_{max}} \sum_{m=-\ell}^{+\ell} Y_{\ell m}^*(\hat{\Omega}_p) Y_{\ell m}(\hat{\Omega}_{p'}) = \delta_{p,p'} \quad (17)$$

where the indices  $p, p'$  label the pixels. For the Healpix pixelization, the number of pixels is given by  $n_{pixel} = 12 \cdot n_{side}^2$  where  $n_{side} = 2^k$  for some integer value of  $k$ . The problem is best seen by considering the discretized orthogonality relation

$$\sum_p \mathcal{A}_p Y_{\ell' m'}^*(\hat{\Omega}_p) Y_{\ell m}(\hat{\Omega}_p) = 0 \quad (18)$$

where  $(\ell, m) \neq (\ell', m')$ ,  $\mathcal{A}_p$  is the area of the pixel  $p$ , and  $\hat{\Omega}_p$  is the position of its center on the celestial sphere.

This relation would be exact in the limit  $p \rightarrow \infty$  where the discrete approximation to the continuum integral becomes exact. However, it is only possible to obtain approximate orthogonality because of the irregularities in the arrangement of the pixels on the sphere. Several pixelization schemes for the sphere have been investigated, and a list of desirable properties may be formulated, but unfortunately no single scheme can be found that simultaneously satisfies all these properties. These properties include:

- (i) To the extent possible, all pixels should have the same shape, which should be as close as possible to a square.
- (ii) The pixels should all have the same area.
- (iii) The pixels should be aligned along azimuthal circles in order to allow the FFT to be employed to speed up the spherical harmonic transform.
- (iv) Passing to a coarser or finer pixelization should be easy to calculate and produce sensible results.

Unfortunately, not all the these requirements can be satisfied, and certain requirements conflict with others.

The problems of pixelizing the sphere have been discussed in the literature by several author and several solutions have been proposed. Crittenden & Turok (1998a,b) proposed an ‘igloo’ pixelization where the pixels have very nearly the same shape. Doroshkevich et al. (2009), on the other hand, proposed another GLESP scheme. Presently the most widely used scheme is Healpix,<sup>1</sup> so we shall restrict our discussion to this scheme under which the sphere is divided into twelve diamonds, which in turn are subdivided into quadrilateral pixels in such a way that the pixels all have exactly equal area and lie on a series of rings of constant latitude, as shown in Fig. 4. Moreover all pixels on a given ring are equally spaced. In this way, when the spherical harmonic transform is carried out, FFTs can be carried out independently on each ring, requiring an effort

<sup>1</sup> <http://healpix.jpl.nasa.gov>

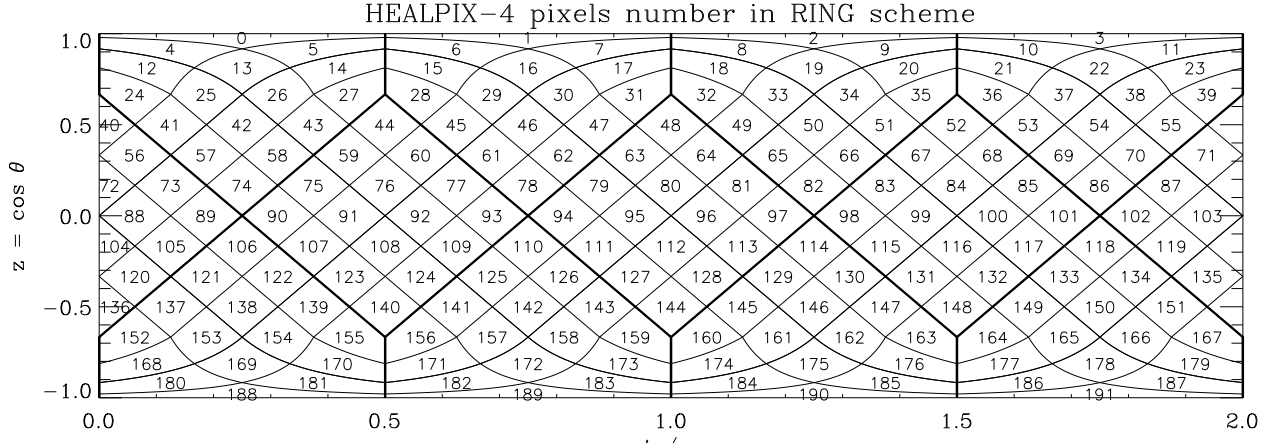


**Figure 4.** In the Healpix scheme the sphere is covered with 12 diamond-shaped regions, which are in turn subdivided into  $n_{side}^2$  pixels where  $n_{side} = 1, 2, 4, \dots$ . Here the upper and lower boundaries each represent a single point. [Reprinted with permission from Gorski et al. (2005)]

of order  $n_{side} \ln(n_{side})$ , thus greatly speeding up the calculation. The most time-consuming part is the  $\theta$  integral, requiring of order  $n_{side}^3$  operations.

Under Healpix the number of pixels per azimuthal ring is constant over a broad band about the equator, and it is only near the poles that the number of pixels per ring starts to drop linearly. Consequently, the pixels near the equator are elongated in the sense along the curves of constant latitude whereas the pixels at mid-latitude are elongated in the opposite sense—that is, along the lines of constant longitude. It is clear that the drop in the number of pixels per ring at high latitudes leads to aliasing errors.

On a rectangular lattice the artefacts of the discretization manifest themselves in a very simple and well-defined way. All power below the Nyquist frequency is represented perfectly and any power above this frequency is aliased down into the band of representable frequencies. On the sphere, by contrast, there is no such sharp demarcation. Small wavenumbers are represented relatively accurately but always with some error. Very large wavenumbers are completely aliased down, but there exists a wide grey zone where limited aliasing occurs. The existence of this intermediate zone is due to the irregular nature of the arrangement of the pixel centers on the sphere, characterized by the lack of an equivalent of the reciprocal lattice.

If we fix  $n_{side}$ , the total number of pixels is  $n_{pix} = 12n_{side}^2$ . In harmonic space for the band  $0 \leq \ell \leq \ell_{max}$  the total number of independent real coefficients is exactly  $(\ell_{max} + 1)^2$ . Each of the rings in the equatorial region contains  $4n_{side}$ . Since representing  $|m| \leq \ell$  requires at least  $(2\ell + 1)$  degrees of freedom, the number of resolution elements per ring is sufficient only for  $\ell$  up to  $(2n_{side} - 1)$ . However, with this choice the harmonic space includes only  $4n_{side}^2$  degrees of freedom, falling short of the  $12n_{side}^2$  by a factor of 3. To match the number of degrees of freedom between the harmonic and pixel spaces we would want (retaining only leading terms)  $\ell_{max} = \sqrt{12}n_{side} \approx 3.5n_{side}$ . So one would want approximately  $7n_{side}$  pixels around the equatorial ring whereas one has only about half that number.

This factor of two discrepancy is explained by two effects. Firstly the pixel shape varies as a function of latitude (and also to some extent as a function of azimuthal position). At the equator the pixel aspect ratio is 1:1.3 whereas on the upper boundary of the equatorial region this ratio is reversed to 1.3:1 approximately. Here the two numbers indicate  $(\Delta\theta) : (\Delta\phi)$ . Near the polar caps the pixel shape becomes increasingly irregular. The second effect is the staggered nature of the pixel center positions between successive rings.

This situation is quite different from that of a rectangular lattice, to which the Nyquist-Shannon sampling theorem can be applied. This theorem states that a band-limited function can be completely recovered, with no error, whenever the density of states implied by the band limit lies below the sampling frequency (which here is the lattice spacing). The key perhaps somewhat artificial assumption is that the function represented is completely band limited, with precisely vanishing contribution from higher frequencies. When this hypothesis is violated, aliasing occurs. Power from higher wavenumbers is down converted to power at lower wavenumbers within the allowed band according to  $\mathbf{k}_{fin} = \mathbf{k}_{RL} + \mathbf{k}_{int}$ , where the wavevector  $\mathbf{k}_{RL}$  belongs to the reciprocal lattice. Since the Shannon-Nyquist theorem applies to one of the two dimensions of the Healpix pixelization scheme, it can be used to shed some light on the pixelization errors that occur when one passes back and forth between the real space pixelized representation and a harmonic representation cut-off by a certain appropriately chosen  $\ell_{max}$ .

Since representing white noise on the pixelized sphere is an essential requirement for the calculations in this paper, we

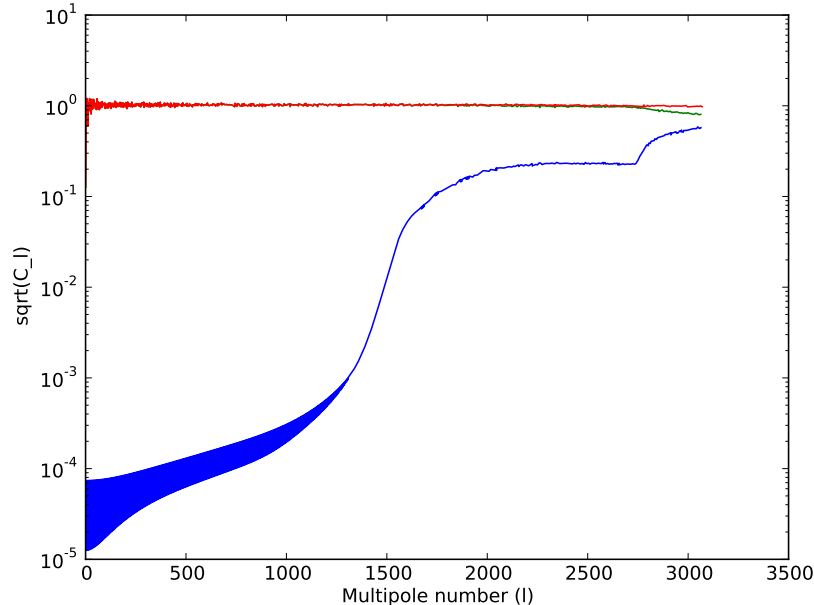


**Figure 5.** We show quantitatively how the pixelized spherical harmonic transform followed by its inverse fails at high wavenumber, on scales of order the interpixel spacing. The red curve represents the input power spectrum of the map  $T$ . After applying the spherical harmonic transform followed by its inverse, a map  $T'$  is obtained, whose power spectrum is shown in green. The power spectrum of the difference map  $\delta T = T' - T$  is shown in blue. Here we have chosen  $\ell_{max} \approx \sqrt{12}n_{side}$  to match the dimension of the pixel vector space and the harmonic space.

illustrate numerically the extent of the difficulties above by generating a map of white noise on the pixelized sphere, denoted as  $T$ , transforming it to harmonic space and back again to obtain  $T'(p) = (S_{inv} \circ S \circ T)(p)$  (where  $S$  and  $S_{inv}$  are the harmonic transform and its inverse, respectively), and examining the difference  $\delta T(p) = T'(p) - T(p)$ . For the harmonic transform with  $n_{side} = 1024$ , we take  $\ell_{max} = 3546$  to make its matrix representation as close as possible to a square matrix. The map  $T'$  has 81% of the power of the original map and the difference map has an rms value per pixel 0.43 (compared to one for the original map), the value that one would expect if the fluctuations of the difference map and of the original map were uncorrelated. The difference map, however, does display some large-scale structure at high Galactic latitude aligned with the joints of the 8 polar diamonds of the Healpix pixelization. In Fig. 5 is shown the power spectrum of the difference map normalized so that  $T(\ell) = 1$ . We observe that the spherical harmonic transform works well as long as the spherical function is band limited as at wavenumbers well below the limit obtained from a simple counting of the number of degrees of freedom.

## 5 INTEGRAL EQUATION FORMULATION IN ANGULAR SPACE

In Sect. 2.2 we discussed the qualitative behavior of the maximum likelihood solution within the masked region under the assumption of an exactly scale invariant power spectrum and no instrument noise. In this section we generalize first to the case of an exactly scale-invariant spectrum with white noise added, and then to the general case where the power spectrum deviates from scale invariance in an arbitrary way. Whereas in the case of exact scale invariance without noise one would obtain an integral equation formulation with a singular kernel, the presence of noise provides the kernel with a nonzero width and deviations from scale invariance provide other interesting structure. We present an integral equation formulation of the problem in this section and show that the kernel is short-range even though there is a falling off tail to arbitrary distance. The special case of an exactly scale-invariant spectrum with no noise could be described as the limit of Gaussian kernels whose width tends to zero.

In order to obtain exact analytic expressions, we assume for the moment an exactly scale-invariant power spectrum for the primordial contribution with perfect white instrument noise, so that

$$\left(\frac{1}{P+N}\right)(\ell) = \left(\frac{A}{\ell^2} + \frac{A}{\bar{\ell}^2}\right)^{-1} = \frac{\bar{\ell}^2}{A} \left[1 - \frac{\bar{\ell}^2}{\ell^2 + \bar{\ell}^2}\right]. \quad (19)$$

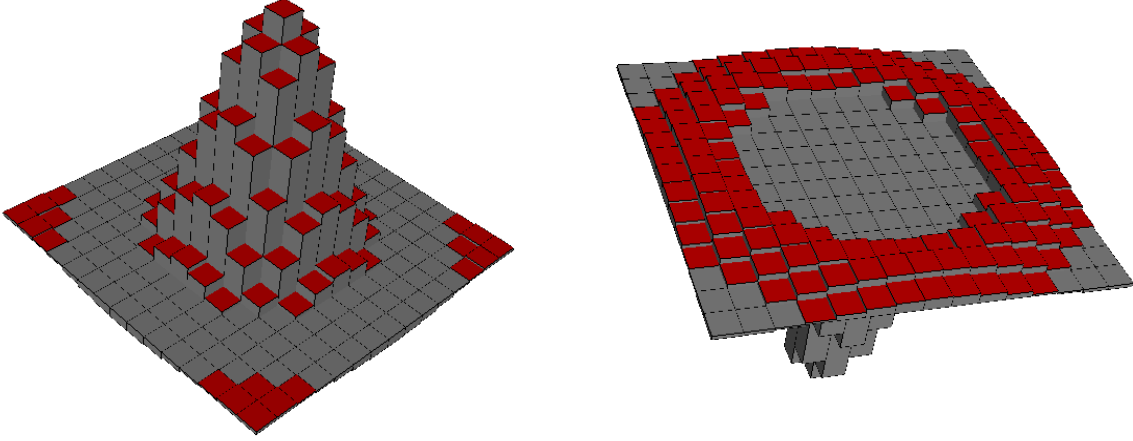


**Figure 6. Maximum likelihood kernel.** We plot the kernel  $\mathcal{K}(r)$  on a grid slightly smaller than  $0.5^\circ$  squared. Each box represents a square pixel of the area (1.72 arcmin) corresponding to the area of an  $n_{side} = 2048$  pixel. Here we have assumed an experiment with a 5 arcmin fwhm resolution and a noise level of  $15\mu K \cdot \text{arcmin}$ , which is slightly better than Planck. More noise and a fatter beam would both widen this kernel. A view from above and below highlight the slight oscillations in the kernel, which has a radius of about  $5'$ .

Here  $\bar{\ell}$  indicates the multipole number where the noise and the primordial signal are equal.

For a realistic power spectrum the kernels would be slightly different and would have to be calculated numerically. It is convenient to assume a continuous random field that has not been pixelized. Here the first term represents the singular part (here a  $\delta$  function) and the second term the smooth regular part. Consequently the probability of a configuration or map  $T(z)$  is proportional to

$$P(T(\mathbf{z})) \propto \exp \left[ -\frac{\bar{\ell}^2}{2A} \int d^2z \int d^2z' T(z) \{ \delta^2(z - z') - \mathcal{K}(|z - z'|) \} T(z') \right] \quad (20)$$

where

$$\mathcal{K}(r) = \bar{\ell}^2 \int \frac{d^2\ell}{(2\pi)^2} \frac{\exp[i\ell \cdot \mathbf{r}]}{\ell^2 + \bar{\ell}^2} = \frac{\bar{\ell}^2}{(2\pi)} \int_0^\infty \frac{t dt J_0(\bar{\ell}rt)}{t^2 + 1} = \frac{\bar{\ell}^2}{2\pi} K_0(\bar{\ell}r). \quad (21)$$

Since

$$(2\pi) \int_0^\infty r dr \mathcal{K}(r) = 1, \quad (22)$$

the convolution with  $\mathcal{K}$  is simply a weighted average over neighboring pixels. We recall the following asymptotic properties of the modified Bessel function  $K_0(w)$ :  $K_0(w) \approx -\ln[w/2] - \gamma$  for  $0 < w \ll 1$  and  $K_0(w) = \sqrt{\pi/2w} \exp[-w]$  for  $w \gg 1$  where  $\gamma$  is Catalan's constant. Note that the logarithmic divergence is very mild and dwarfs the factor  $r$  in the area element, so the bulk of the weight of this average arises from pixels a distance of order  $\bar{r} = \bar{\ell}^{-1}$  from the center. The kernel dies off as  $\exp[-r/\bar{r}]$ , so filling in is an extremely local process in this special case. We will see that for more realistic power spectra (e.g., with acoustic peaks) the fall-off is less rapid.

It is convenient to split  $\mathbf{z}$  into masked and unmasked (or equivalently unobserved and observed) pixels  $\mathbf{z} = (\mathbf{x}, \mathbf{y})$ . As discussed earlier, the bottleneck in carrying constrained Gaussian realization is finding  $\mathbf{x}_{ML}$  given a set of values for  $\mathbf{y}$ . We want to find  $\mathbf{x}_{ML}$  given values for  $\mathbf{y}$  so that the integral in the exponential of eqn. (20) is minimized. A necessary and sufficient condition is that for all  $\mathbf{x}$

$$T(\mathbf{x}) = \int d^2z \mathcal{K}(|\mathbf{z} - \mathbf{x}|) T(\mathbf{z}) \quad (23)$$

where the integral over  $\mathbf{z}$  includes masked and unmasked pixels alike. In Fig. 6 the numerically computed kernel for the Planck experiments is shown assuming the instrument specification given in the caption and the 7-year WMAP best-fit cosmological model rather than the idealized assumptions above. Figs. 7 and 8 show the shapes of the kernels for the Planck noise level and also several boosted noise levels.

The short-range character of the kernel makes manifest that filling in is a relatively local process, despite the fact that low- $\ell$  multipoles contribute substantially to the values inside the widely separated holes. Widely separated holes can be filled in independently with very little error because their coupling decays as  $\exp[-d/\bar{r}]$ . The problem of coupling may in principle

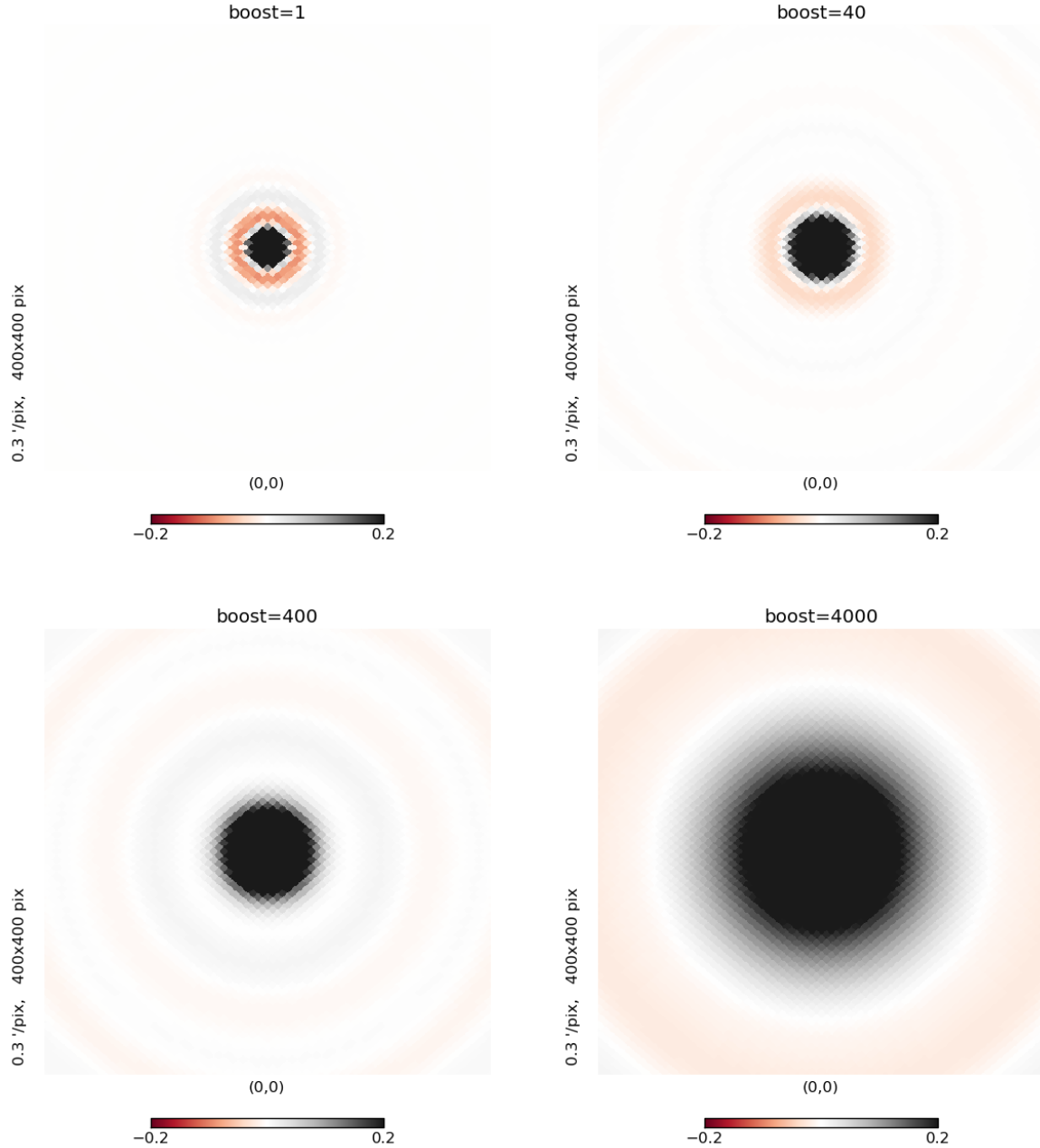


**Figure 7. Kernels for maximum likelihood filling in.** From left to right and then top to bottom we show the kernels with the instrument noise boosted by factors of 1, 40, 400, and 4000, respectively. The square patches are 120 arcmin on a side. A color scale has been chosen so that white corresponds to a vanishing value, redish hues to negative values, and greyscale hues to postive values. The kernel maximum has been normalized to +1 and the color scale saturates at  $\pm 0.2$  in order to emphasize the oscillations surrounding the central peak. The size of the central peak, which has no interesting structure, is exaggerated by saturation effects. The individual pixels resulting from an  $n_{side} = 2048$  pixelization are clearly visible.

be solved iteratively by generating a sequence of maps  $T^{(i)} = (T_x^{(i)}, T_y^{(i)})$  where

$$T_x^{(i+1)}(\mathbf{x}) = \int d^2 z \mathcal{K}(|\mathbf{z} - \mathbf{x}|) T^{(i)}(z). \quad (24)$$

This is akin to Gauss-Seidel iterative relaxation for elliptic PDEs approximated using a finite-difference scheme.

Now we pass to some orders of magnitude first assuming a single isolated hole of dimension  $D$ . The convergence of the

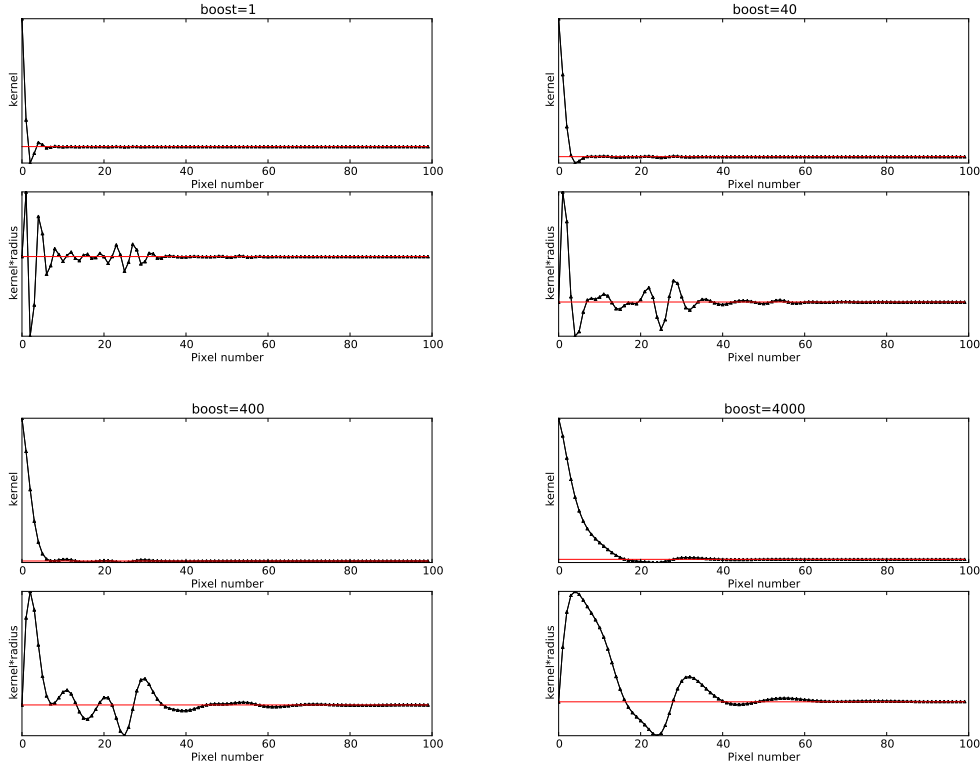


**Figure 8. Kernels for maximum likelihood filling in.** For the same kernels as in the previous plot we show the radial profiles, first plotted as  $K(r)$  and then as  $r \cdot K(r)$  to highlight the radial oscillations and to give a weighting that includes the effect of the volume element. For the kernel with unboosted noise the oscillations have an important effect whereas for the boosted kernels the effect of the oscillations is less important.

algorithm in eqn. (24) would be controlled by the dimensionless parameter  $\lambda = (D/\bar{r})$ . The convergence is roughly geometric after an initial transient, and the number of steps required for convergence scales as  $O(\lambda^2)$ . For holes of oblong dimensions (e.g., an elongated rectangle or even an infinite strip), it is the smaller dimension that should be used for  $D$  in the expression for  $\lambda$ . The convergence scales as  $\lambda^2$  because settling down is essentially a diffusive process, where the random step per iteration is  $\bar{r}$ .

Eqn. (23) is remarkably similar to a relation for solutions to Laplace’s equation in two dimensions, where

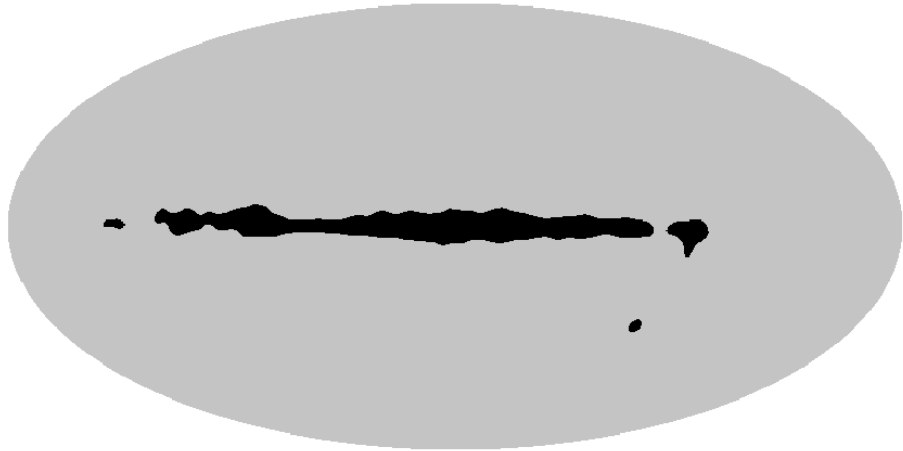
$$\phi(x, y) = \int_0^{2\pi} \frac{d\theta}{2\pi} \phi(x + \rho \cos \theta, y + \rho \sin \theta) \quad (25)$$

whenever the disk of radius  $\rho$  about  $(x, y)$  lies entirely within the domain where Laplace’s equation is satisfied. For a harmonic function, because of the above relation and the symmetry of the kernel, eqn. (23) would automatically hold.

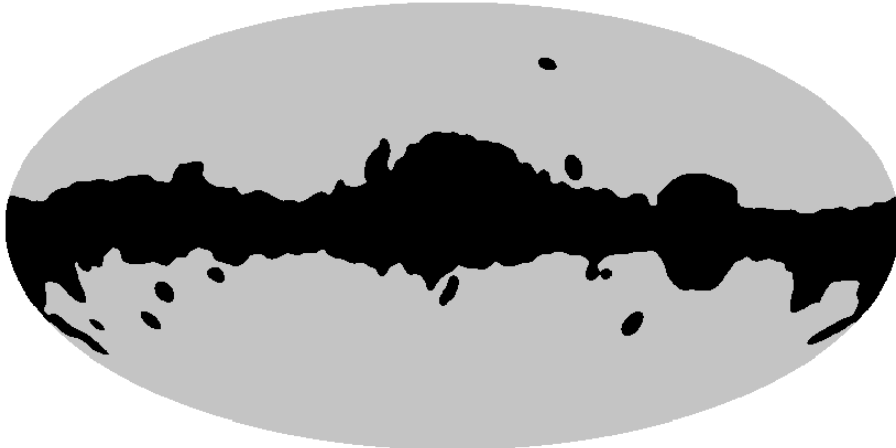
This analogy suggests that the farther one goes into the interior of a masked region, staying several lengths  $\bar{r}$  from the boundary, the maximum likelihood reconstructions looks increasingly like a solution to the Laplace equation, for which any kernel is sufficient to reconstruct the interior. This feature suggests a method of accelerating the convergence of eqn. (24) with very little error. The idea is to use in the far interior kernels fatter than  $\mathcal{K}$  to accelerate the propagation, or diffusion, of information from the boundary region into the interior. It is only within the boundary layer (within a few lengths  $\bar{r}$  from the unmasked region) that we expect significant deviations from Laplace type behavior, because the kernel looks beyond the boundary.

## 6 A PRACTICAL FILLING IN PROCEDURE FOR FULL-SKY SPHERICAL MAPS

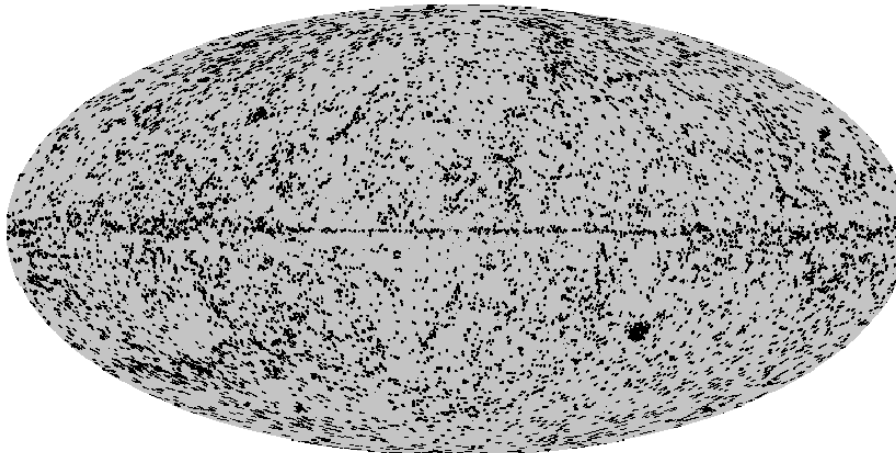
Fig. 9 shows three representative masks of the sort likely to be used for the Planck analysis. From top to bottom are shown: (a) a mask cutting out a modest portion of the galaxy, (b) a more aggressive Galactic mask, and (c) a point source mask. In order to define the filling in problem, we must also set a level for the instrument noise. The filling in problem is numerically



(a)



(b)



(c)

**Figure 9. Three candidate Planck masks.** In panels (a) and (b) the Galactic plane is masked out less and more aggressively and in panel (c) a mask for the discrete sources of the Planck ESRC is shown. *(Courtesy of Jacques Delabrouille and Guillaume Castex)*

more demanding for smaller values of the instrument noise. Therefore we adopt a beamwidth of  $5'$  (fwhm) for all the channels and combine the 100 GHz, 143 GHz, and 217 GHz channel sensitivities in quadrature and assume a 30 month survey to obtain a white noise level of  $15\mu K \cdot \text{arcmin}$  in order to formulate a test problem slightly more difficult than what will be encountered by Planck. As discussed previously, the most challenging mask is (b) with the wide Galactic cut. Since the width of the kernel is of order  $6'$  and that of the cut is about  $40^\circ$ ,  $\bar{\lambda} = 400$  and the number of iterations required for converge would be of order (few)  $\times 10^6$  using the iterative rule in eqn. 24. This is clearly impractical except for perhaps narrow point source masks. Therefore an approach based on Gauss-Seidel iteration is not feasible.

In this section we describe a two-part procedure. First the far interior of the large holes is filled using a Laplace solver especially suited to domains of the pixelized sphere with irregular boundaries. We already showed in Sect. 5 why the Laplace equation holds asymptotically as one passes into the far interior of the masked region. In the next subsection we investigate this question quantitatively to determine exactly how far into the interior one must go for this to be an accurate approximation. Then we describe the details of our fast Laplace solver for the pixelized sphere. The Laplace approximation is good as long as the scales over which the maximum likelihood solution varies is large compared to the width of the exact kernel. As one passes farther into the interior, the small scale structure on the boundaries decays away and this becomes a better and better approximation. But as one approaches the boundaries of the masked regions, the length scale of the fluctuations becomes smaller and smaller almost in a fractal way (until the noise acts as a cutoff). The central region of the kernel primarily describes the effect of the noise, and the oscillations in the tail where the kernel takes negative values reflect the acoustic oscillation structure. That this qualitative description is correct is clearly illustrated by the preconditioned conjugate gradient solutions on a flat domain discussed in Sect. 3 and shown in Fig. 3. (See in particular the zoom of the mask boundary.) See also Fig. 13.

The second step of our procedure corrects the approximate solution near the boundary by using a kernel to improve the small-scale structure between the far interior region and the unmasked region. The kernel captures those aspects of the maximum likelihood not well approximated by the Laplace approximation. If these strips are too wide, the condition number  $\kappa$  of the resulting linear system is too large, and we cannot achieve convergence within a feasible number of iterations. We use several strips of decreasing width and artificially boost the noise to reduce the condition number on all but the last and narrowest strip. In this way information about the power spectrum on larger scales can be taken into account but the small scale structure is washed out. In the later strips closer to the boundary with less noise the correct small scale structure is restored. Fig. 13 illustrates this noise boosted kernel procedure on a strip  $2.9^\circ$  wide on the celestial sphere.

### 6.1 Accuracy of Laplacian approximation in far interior of masked region

In Section 5 drawing inspiration from an exact analytic expression for the kernel, we argued that in the far interior of the masked region—that is, a few times  $\bar{r}$  away from the boundary—the maximum likelihood solution should be well approximated by a solution to the Laplace equation. To test this assertion we must establish an appropriate figure of merit for evaluating this approximation. The most appropriate test is to propagate boundary values into the interior of a region lying completely within the far interior of the large hole assuming Laplace’s equation and compare to a reliable numerical solution calculated using the conjugate gradient method.

The Laplace interpolation from the boundary of a periodic rectangular strip can be calculated in a very simple way. Suppose that we want to solve the Laplace equation on a cylinder with  $0 \leq x \leq a$  where  $x = 0$  and  $x = a$  are identified and  $0 \leq y \leq b$ . The solution may be continued from the two boundaries into the interior using

$$\phi(x, y) = \sum_{m=-\infty}^{+\infty} \int_0^a \frac{dx'}{a} \exp[im(2\pi/a)(x - x')] \left[ \frac{\sinh[(2\pi m/a)(b - y)]}{\sinh[(2\pi m/a)b]} \phi(x', y = 0) + \frac{\sinh[(2\pi m/a)y]}{\sinh[(2\pi m/a)b]} \phi(x', y = b) \right]. \quad (26)$$

For a pixelized surface with  $N$  points in the  $x$  direction, the sum becomes restricted from 0 to  $(N - 1)$ .

In Fig. 3 we showed a setup on the torus designed to mimic the problem of filling in an aggressive Galactic cut. In Fig. 10 we show how the exact solution compares with the Laplace solution on the domain resulting after  $2^\circ$  along each of the boundaries has been removed from the originally  $20^\circ$  wide strip. The left, middle, and right panels show the exact conjugate gradient solution, the Laplace solution, and the difference map, respectively. We observe that the error is very small. We see that the Laplace equation is a very good approximation in the far interior.

### 6.2 Automatic domain definition in the masked region

One of the required tasks, both for the Laplace solver and the noise-boosted kernel improvement of the solution near the boundary, is to subdivide the masked region into subdomains consisting of points closer than a certain distance  $\delta$  from the boundary. Let us call the unmasked, visible region  $R_0$ . We define a boundary layer  $R_1$  consisting of those pixels within a

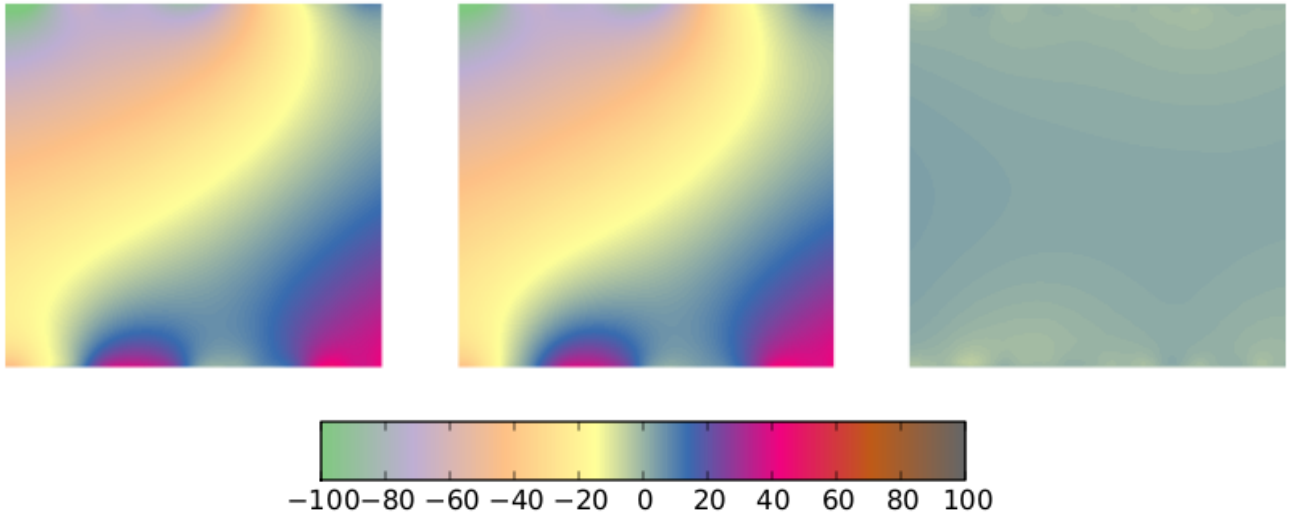


**Figure 10. Laplace’s equation as an approximation for the far interior of the hole.** We demonstrate how well Laplace’s equation is satisfied in the far interior of a large masked region, here the  $40^\circ$  cut, by cutting away the boundary region  $2^\circ$  wide, as shown in the left panel, and using the boundary data here on top and below combined with Laplace’s equation to calculate an interior solution, shown in the middle panel. The right panel shows the difference, which is small ( $< 5\%$ ).

distance  $\delta_1$  of  $R_0$ . Masks to avoid the galaxy and point sources are often quite irregular and complicated in shape, so a robust automatic procedure is needed for subdividing the mask. We calculate  $R_1$  by setting all the pixels in  $R_0$  equal to one and all the pixels in its complement equal to zero. Then we convolve this map with a top hat kernel of radius  $\delta_1/2$ , and all the pixels with a positive value and not in  $R_0$  belong to  $R_1$ . Those farther in the interior should be still null after the convolution. In practice a small positive threshold (which we choose equal to 0.03) is used to avoid numerical artifacts. This procedure is repeated to partition points in the masked domain into a number of subdomains according to their closest distance from the boundary. The result of the subdivision of the masked region for the combined Galactic and point source masks in Fig. 9 is shown in Fig. 11.

### 6.3 Laplace solver

There are many ways to solve the Laplace equation on a discretized domain (e.g., multigrid, finite-element methods, etc.), but for the present problem the choice of method is dictated by the irregular nature of the boundary. A method is needed that will work with a mask defined as a boolean function defined on a pixelized sky. The method described below closely resembles multi-grid but is kernel based so that it can easily be implemented on the pixelized sky. The most naive method—relaxation across neighboring pixels—would require of order  $w^2$  iterations where  $w$  is the width of the domain measured in pixels. We require a method that converges in a number of iterations of order a power of  $\log(w)$ . This rapid convergence is achieved by employing a series of kernels of varying radius. We depart from the observation that the value of a harmonic function in a circle is equal to the average value of the function on the circumference. Consequently, in solving by relaxation one wants to update values in the interior by using the largest circle that does not extend outside the masked domain. We also need to propagate information from the boundary into the interior and this is done by allowing the points very near the boundary to average over pixels lying slightly outside. Two other considerations enter. On the sphere the only efficient way to compute convolutions is by using harmonic transforms. Therefore a small number of kernels is used whose radii vary according to a geometric progression. Also the kernels profiles are chosen to be annular with a finite width and solid for the very smallest in order to avoid errors associated with Gibbs oscillations and inaccuracies of the spherical harmonic transform on the scale of the pixelization. [See Fig. 12]

### 6.4 Improvement of the solution near the boundary

Starting with a map filled in using the Laplace solver, we improve the solution near the boundary of the masked region where the kernel profile becomes increasingly relevant. We define a series of strips  $D_1 \supset \dots \supset D_n$  consisting of pixels a distance

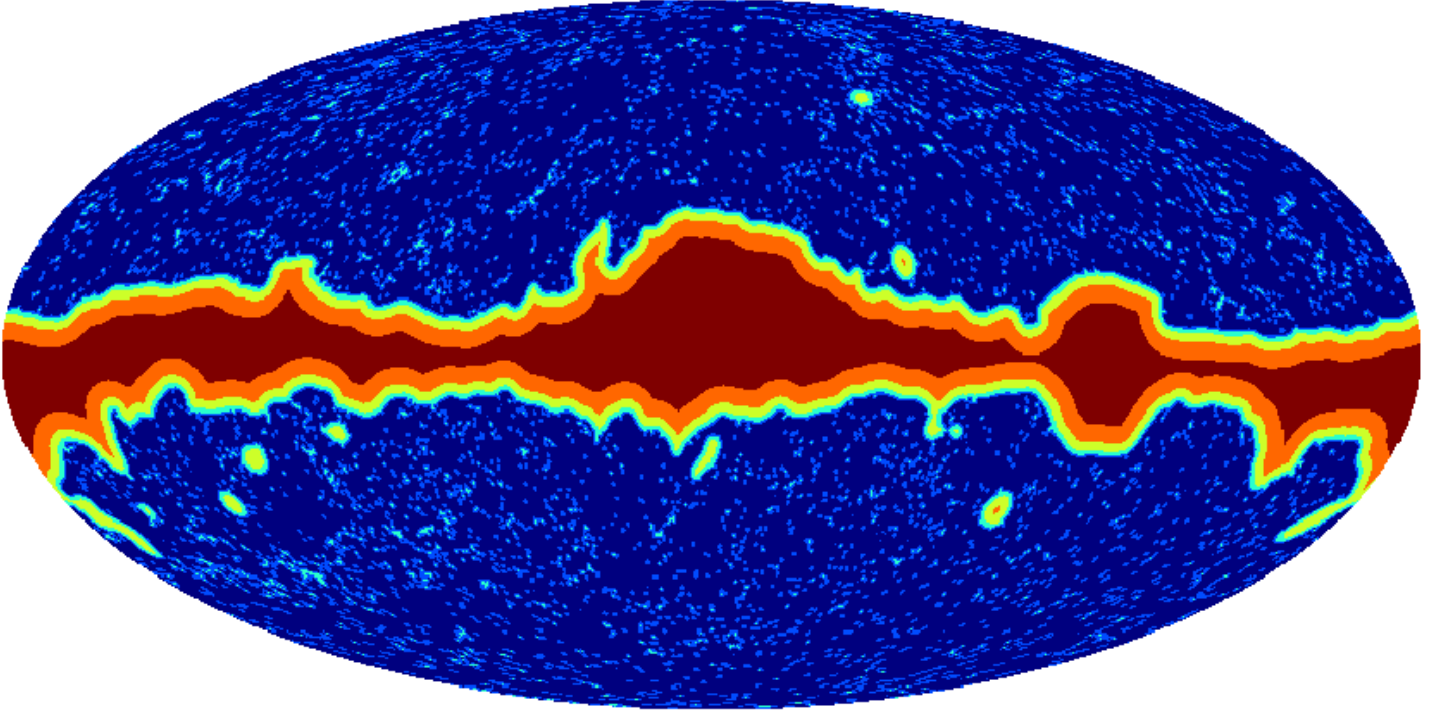


**Figure 11. Subdivision of masked sky according to distance from unmasked region.** For the kernel based methods of solving the Laplace equation in the masked region using the data in the unmasked region as boundary data and for the improvement of the maximum likelihood solution near the boundary using the exact kernel and kernels with boosted noise, it is essential to subdivide the masked region into subregions according to distance from the unmasked region. Here is shown the result of the algorithm described in the text. The dark blue is the unmasked region and the regions going from light blue to redish brown are subregions farther and farther from the boundary.

$w_1 > \dots > w_n$  within the boundary, respectively, and the noise is boosted by a factor of  $\beta_1 > \dots > \beta_n = 1$ . The condition number of the resulting linear equation depends on both the width of the strip and the noise boost  $\beta$ . The value of the largest eigenvalue is very nearly one. This corresponds to small-scale structure annihilated by  $K$  so that  $(I - K)$  acts very nearly as the identity operator on small scales. Large scale configurations, on the other hand, lead to small eigenvalues. The regularization of the smallest eigenvalues (so that they do not lie too close to zero) can be interpreted as leakage from the boundary. For very large-scale structure,  $K$  acts almost as the identity, because the integral over the kernel is unity. However near the boundary, leakage takes place. On a long narrow strip the eigenfunction has approximately a sine function transverse profile, and the lowest eigenvalue (or equivalently the inverse of the condition number) is of order  $(d/w)^2$  where  $d$  is the effective width of the kernel, which is fattened as  $\beta$  is increased. Note that the effective width may be much smaller than the actual support of the kernel because of oscillations of the kernel as seen above.

A key input to choose the parameters of our method is approximating the condition number of the linear system resulting for a given power spectrum and instrument noise pair as a function of strip width and noise boost factor. We used a Lanczos method to determine the condition number. The basic approach is to generate a Krylov space in much the same way as for the conjugate gradient method choosing a basis such that matrix  $(p_i, Ap_j)_A$  is triadiagonal. Here the directions  $p_i$  are A-conjugate. The range of the eigenvalues of this subspace are supposed to be representative of the range for the full matrix  $A$ . After a reasonable number of iterations, the maximum and minimum eigenvalues of the matrix, calculated using a standard  $QR$  algorithm, converge. (See Golub & Van Loan (1996) for a nice overview of Lanczos methods.) A knowledge of the condition number is invaluable both for predicting the rate of convergence and formulating a suitable stopping rule.

We chose our sequence so that  $\beta$  descends to one following more or less a geometric progression and  $w$  is adjusted to obtain a condition number in the neighborhood of  $10^2$ . In this way 20 iterations per strip of the conjugate gradient method were found to suffice. Our values of  $(\beta, w)$  where (2000, 100), (400, 35), (40, 15), (1, 7). Fig. 13 shows the final result starting on a strip of width 100 pixels.

The above method alone with the parameters chosen would work for holes and masks of width no larger than  $1.5^\circ$ . But realistic Galactic masks are typically much larger than this, up to  $40^\circ$  wide or more. One option would be to start the sequence

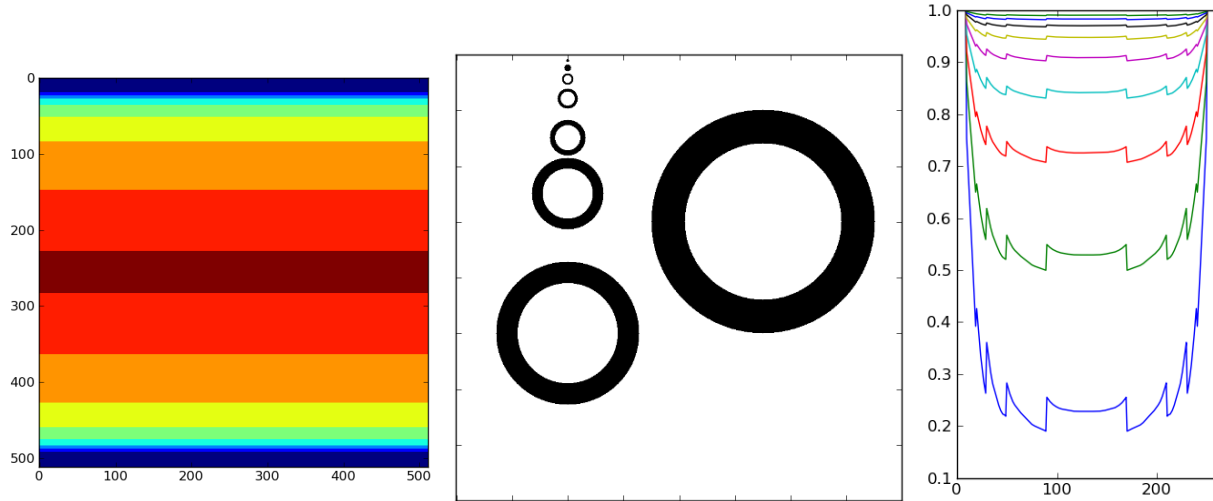


**Figure 12. Laplace solver scheme.** The Laplace solver described in the text uses 9 kernels of various widths (shown in the middle panel). The left panel shows the unmasked region (in dark blue) and several nested subregions of increasing distance from the boundary. Only in the first very thin subregion is the kernel allowed to extend into the unmasked region (in order to transmit the boundary data in the edge of the masked region). In all but the outermost of the masked subregions the largest kernel that does not extend into the unmasked region is used to update the interior data by replacing a value with the average over the kernel. The rightmost panel illustrates the convergence with successive iterations. The jaggedness arises from the discontinuous change in the choice of kernel as one passes from one subregion into the neighboring subregion. Here the boundary data was set to one and the interior values to zero as an initial condition. Numerous other tests with varying wavenumber for the boundary data were carried out to validate the accuracy of the method and characterize its convergence properties.

with additional strips with even larger noise boost factors and widths. We instead chose to capitalize on the fact that in the far interior the maximum likelihood solution very nearly solves the Laplace equation.

## 6.5 Validation of above procedure

We validated the procedure described in the previous subsections by comparing to solution obtained using a direct method (i.e., Gaussian elimination) for solving the linear system  $((\mathbf{C}^{-1})_{\mathbf{xx}})\mathbf{x} = ((\mathbf{C}^{-1})_{\mathbf{xy}})\mathbf{y}$  where  $\mathbf{x}$  denotes the vector of masked pixels. We used a square mask of 100 pixels on a side centered on the equator. The direct method, whose computational complexity scales as  $n_{masked}^3$ , is still feasible on a domain of this size and has the advantage that it can deal with the large condition number of the matrix  $(\mathbf{C}^{-1})_{\mathbf{xx}}$  without difficulty. In Fig. 14, we compare the maximum likelihood solution using both methods. The agreement is quite good but not perfect. We have not fully explored the optimization of the parameters governing the improvement along the boundary of the masked region. As the strips become wider (entailing a larger condition number and hence requiring more iterations), the approximate solution becomes increasingly accurate. A study of the accuracy required for probes of primordial non-Gaussianity as well as a comparison with competing methods of filling in, which unlike the present one are non-Gaussian, will be addressed in a forthcoming publication [Bucher, Louis & van Tent (2011)].

## 7 CONCLUDING REMARKS

We have demonstrated a workable filling in procedure for masked regions of arbitrary width on the pixelized sphere, which we have validated using a Healpix pixelization of  $n_{side} = 2048$ . There is no reason why the methods developed here should not extend to even finer pixelizations because the dimensionless ratios defining the numerical difficulty of the problem do not involve the overall size of the sphere. Moreover for the Laplace solver presented here the number of iterations needed scales as a power of the logarithm of the ratio of two angular scales, allowing wide masks to be treated with only a very modest increase in the number of iterations as will be necessary for very aggressive Galactic cuts.

As explained in Section 2.3, the hardest part of realizing constrained Gaussian realizations is calculating the maximum likelihood for the missing pixels because the random component can be computed using the method introduced by Hoffman once one has a working and efficient procedure for calculating the maximum likelihood configuration.

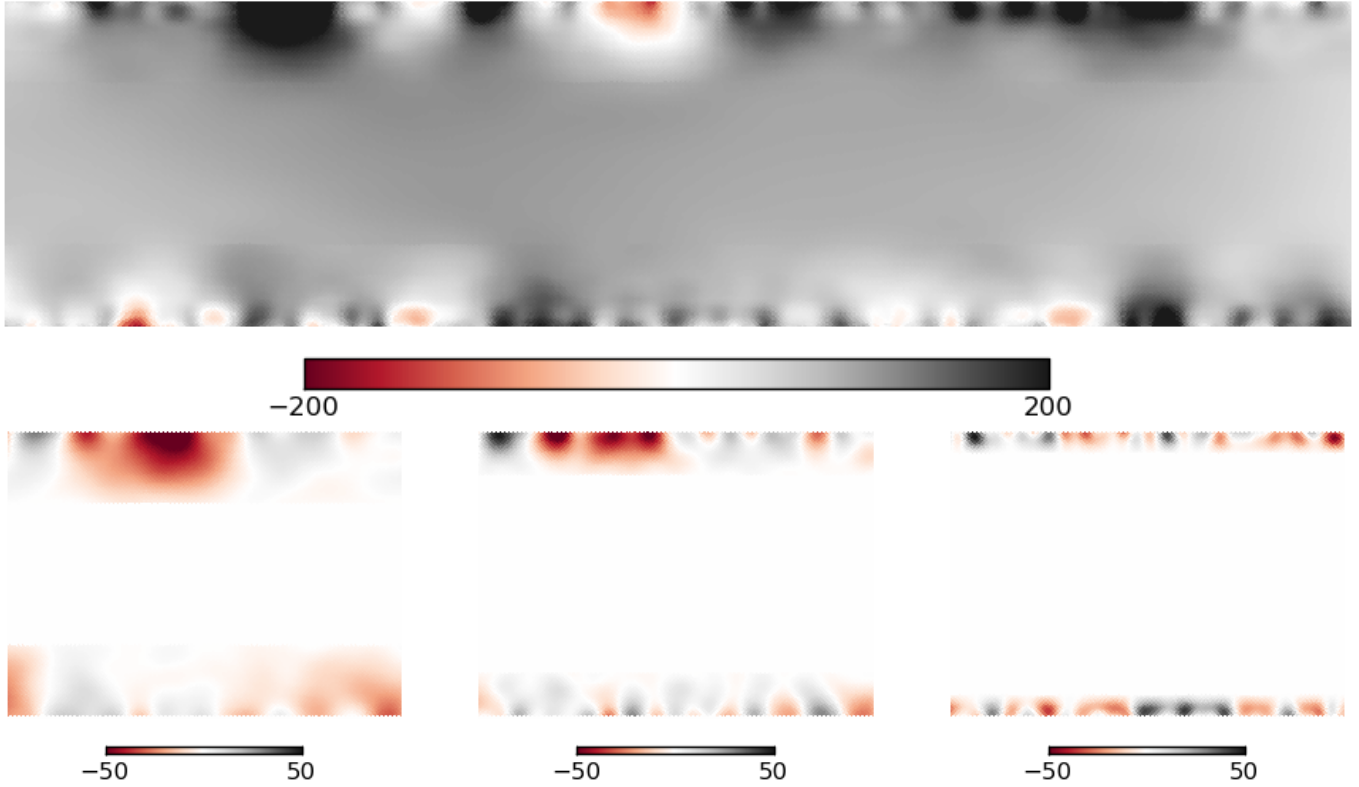


**Figure 13. Filling in on the sphere.** We show the maximum likelihood filling in of  $2.9^\circ$  ( $\approx 100$  pixel) wide equatorial strip of the celestial sphere pixelized using Healpix at  $n_{side} = 2048$  resolution using the parameters described in the text. First the filling in is carried out assuming a noise level boosted by 2000 in order to fill in the large scale structure in the middle of the strip. Then the regions near the boundaries are corrected to fill in the small scale structure by a sequence of three refinements across narrow strips just above and below the upper and lower boundaries. The widths and noise boosts of these strips are  $(\beta_{noise}, w_{pixels}) = (400, 35)$ ,  $(40, 15)$  and  $(1, 7)$ . The bottom three panels show the difference maps between successive iterations (left) to (right).

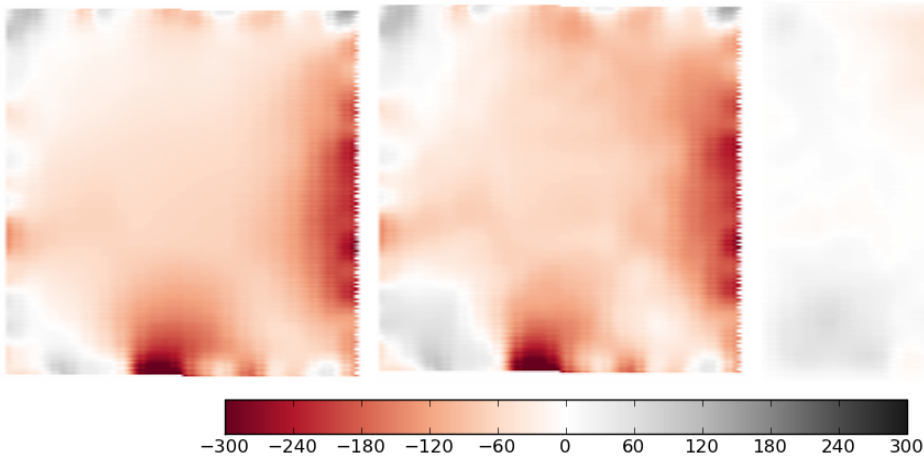


**Figure 14. Validation of approximate solution.** From left to right we show the approximate solution calculated according to the procedure described in Sects. 6.2-6.4, the exact solution calculated using a direct method (i.e., Gaussian elimination) to solve the linear system using the exact kernel on the entire domain, and the difference map. The size of the domain is  $100^2$  pixels in the  $n_{side} = 2048$  Healpix pixelization.

One of the disappointing conclusions of this study is that the preconditioned conjugate gradient method that we successfully implemented on a comparable flat domain with periodic boundary conditions did not work when carried over to the sphere. The difference between the two cases is difficult to understand and plausibly attributable to the difficulties of implementing a spherical harmonic transform and its inverse as discussed in Section 4.

One interesting feature of the methods introduced in this paper are that they are kernel based and thus to some extent independent of the pixelization used. The basic operation is convolving maps with kernels, so even though the maps used are pixelized there is no implicit finite difference scheme involved. The only requirement is that the pixelization be fine enough so that the convolutions calculated are sufficiently accurate. It is interesting that the idealization of white instrument noise allows us to analyze what is going on independent of any pixelization.

A code to carry out the procedures as described in the text is available from the authors upon request.

## 8 DISCUSSION

**Acknowledgements:** We would like to thank Jean-Francois Cardoso, Joanna Dunkley, and Bartjan van Tent for useful discussions and Jacques Delabrouille and Guillaume Castex for providing Galactic and point source masks for testing our code. The authors acknowledge the use of the Healpix package Gorski et al. (2005) and the healpy python interface (<http://code.google.com/p/healpy/>) written by Cyrille Rosset for many of the computations carried out in this work. . TL acknowledge the use of Flipper code for flat sky maps analysis.

## REFERENCES

- P. Abrial , Y. Moudden , J. L. Starck , B. Afeyan , J. Bobin , J. Fadili , M. K. Nguyen, “Morphological Component Analysis and Inpainting on the Sphere: Application in Physics and Astrophysics,” *J. Four Anal and Applications (JFAA)*, 6, 729 (2007) ([http://jstarck.free.fr/sphMCA\\_revised\\_20070823.pdf](http://jstarck.free.fr/sphMCA_revised_20070823.pdf))
- P Abrial, Y Moudden, JL Starck, J Fadili, J Delabrouille & M Nguyen, “CMB data analysis and sparsity,” *Statistical Methodology* 5, 289 (2008) (arXiv:0804.1295)
- M Bucher, T Louis & B van Tent, “Stress tests for CMB filling in algorithms,” (in preparation)
- E Bunn, Y. Hoffman & J. Silk, “The Wiener filtered COBE DMR Data and predictions for the Tenerife experiment,” *Ap. J.* 461, 1 (1996);
- E Bunn, K Fisher, Y Hoffman, O Lahav, J Silk, & S Zaroubi, “Wiener filtering of the COBE Differential Microwave Radiometer data,” *Ap.J.* 425, 359 (1994)
- E Bunn, Y Hoffman & J Silk, “The effects of incomplete sky coverage on the analysis of large angular scale microwave background anisotropy,” *Ap.J.* 425, 359 (1994)
- JF Cardoso & S Prunet, “Spherical inpainting,” *in Proceedings Mathematical Methods for Multi-Channel Image Processing (MultIm2006)*, Beijing, 2006.7.7-8
- RG Crittenden & NG Turok, “Exactly azimuthal pixelizations of the sky,” (astro-ph/9806374)
- R Crittenden, “Igloo Pixelizations,” *Astrophys. Lett. Commun.* 37 (2000) 377 (astro-ph/9811273)
- S Das, T Marriage et al., “The Atacama Cosmology Telescope: A Measurement of the Cosmic Microwave Background Power Spectrum at 148 and 218 GHz from the 2008 Southern Survey,” *Ap. J.* 729, 62 (2011) (arXiv:1009.0847)
- A Doroshkevich et al., “The Gauss-Legendre Sky Pixelization for the CMB polarization (GLESP-pol): Errors due to pixelization of the CMB sky,” (arXiv:0904.2517)
- J Dunkley, R Hlozek, J Sievers et al., “The Atacama Cosmology Telescope: Cosmological Parameters from the 2008 Power Spectra,” (arXiv:1009.0866) (submitted to Ap.J.)
- F Elsner & B Wandelt, “ARKCoS: Artifact-Suppressed Accelerated Radial Kernel Convolution on the Sphere,” (2011) arXiv:1104.0672v1 [astro-ph.IM]
- H Erikson, I O’Dwyer, J Jewell, B Wandelt, D Larson, K Gorski, S Levin, A Banday & P Lilje, “Power spectrum estimation from high-resolution maps by Gibbs sampling,” *Ap. J. Supp.* 155, 227 (2004) (astro-ph/0407028)
- H Eriksen, J Jewell, C Dickinson, A Banday, K Gorski & C Lawrence, “Joint Bayesian component separation and CMB power spectrum estimation,” *Ap. J.* 676:10 (2008) (astro-ph/0709.1058)
- S Feeney, H Peiris & A Pontzen, “Avoiding bias in reconstructing the largest observable scales from partial-sky data,” (astro-ph/1107.5466)
- R Fletcher, “Conjugate gradient methods for indefinite systems,” *Lecture Notes in Mathematics* 506, 73 (1976)
- GH Golub & CF Van Loan, *Matrix computations* (3rd edition), (Baltimore: Johns Hopkins University Press, 1996)

- KM Gorski, E Hivon, AJ Banday, BD Wandelt, FK Hansen, M Reinecke & M Bartelman, "HEALPix: A framework for high resolution discretization and fast analysis of data distributed on the sphere," *Ap.J.* 622, 759 (2005) (astro-ph/0409513)
- K Gorski, B Wandelt, F Hansen, E Hivon, & A Banday, "The HEALPix Primer," (arXiv:astro-ph/9905275)
- MR Hestenes & E Stiefel, "Method of conjugate gradients for solving linear equations," *J. Res. Nat. Bur. Stand.* 49, 409 (1952)
- Y Hoffman & E Ribak, "Constrained realization of Gaussian fields: a simple algorithm," *ApJ (Lett)* 380, L5 (1991)
- R Keisler, C Reichardt et al., "A Measurement of the Damping Tail of the Cosmic Microwave Background Power Spectrum with the South Pole Telescope," (astro-ph/1105.3182) (submitted to *Ap.J.*)
- K Inoue, P Cabella, & E Komatsu, "Harmonic inpainting of the cosmic microwave background sky: formulation and error estimate," (astro-ph/0804.0527)
- PF Muciaccia, P Natoli & N Vittorio, "Fast Spherical Harmonic Analysis: A Quick Algorithm for Generating and/or Inverting Full-Sky, High-Resolution Cosmic Microwave Background Anisotropy Maps," *Ap J Lett* 488, L63 (1997) (astro-ph/9703084)
- L. Perotto, J. Bobin, S. Plaszczynski, JL Starck & Lavabre, A. "Reconstruction of the cosmic microwave background lensing for Planck," *A& A* 519, 4 (2010)
- R van de Weygaert & E Bertschinger, "Peak and gravity constraints in Gaussian primordial density fields: an application of the Hoffman-Ribak method *MNRAS* 281, 84 (1996) (astro-ph/9507024)
- B Wandelt, D Larson & A Lakshminarayanan, "Global exact cosmic microwave background data analysis using Gibbs sampling," *Phys. Rev. D* 70 (083511) (2004)
- S Zaroubi, Y Hoffman, K Fisher & O Lahav, "Wiener Reconstruction of the Large-Scale Structure," *Ap.J.* 449, 446 (1995) (arXiv:astro-ph/9410080)